國立交通大學

電子工程學系 電子研究所

碩士論文

人體通道通訊系統平台之設計

Design of Body Channel Communication Emulation Platform

研 究 生: 林恕平

指導教授: 李鎮宜 教授

中 華 民 國 一百零一 年 十 月

人體通道通訊系統平台之設計

Design of Body Channel Communication Emulation Platform

研 究 生: 林恕平　　Student： Shu-Ping Lin

指導教授: 李鎮宜 教授　　Advisor： Prof. Chen-Yi Lee

國 立 交 通 大 學

電子工程學系 電子研究所

碩 士 論 文

A Thesis
Submitted to Department of Electronics Engineering and
Institute of Electronics
College of Electrical and Computer Engineering
National Chiao Tung University
in partial Fulfillment of the Requirements
for the Degree of
Master
in
Electronics Engineering

October 2012
Hsinchu, Taiwan, Republic of China

中華民國 一百零一 年 十 月

人體通道通訊系統平台之設計

學生：林恕平　　　　　　　　指導教授：李鎮宜 博士

國立交通大學

電子工程學系 電子研究所

摘要

人體通道通訊是一項利用人體表面皮膚傳輸訊號之科技。其具有高導通性、低傳輸頻率，以及限制訊號之傳輸於人體周遭等特性。這些特性使人體通道通訊特別適合用於多媒體影音下載、行動健康看護系統，以及門禁控制和結帳系統等應用。

為了達到低能耗之高速率傳輸、小面積，以及提供使用者舒適之佩戴，本論文設計之人體通道通訊系統使用正交分頻多工傳輸策略以及無石英震盪器。因無石英震盪器之頻率誤差較大，亦設計對應之頻率校正方法。

本論文呈現一使用正交分頻多工傳輸策略以及無石英震盪器之人體通道通訊系統平台。系統平台包含傳送端前端電路、接收端前端電路，以及基頻收發器。系統平台目前可以達到6.7Mbps之穩定高速傳輸。

Design of Body Channel Communication Emulation Platform

Student: Shu-Ping Lin   Advisor: Dr. Chen-Yi Lee

Department of electronics engineering and Institute of electronics,

National Chiao Tung University

Abstract

Body channel communication (BCC) is an emerging technology which uses skin of human body as transmission channel. It has advantages such as high conductivity, low transmission frequency, and the confinement of transmission signal to the body area. With those advantages, BCC is very suitable for applications such as multimedia downloading, access control and payment, and mobile health-care, and so forth.

In order to get high data rate with low operation energy, as well as to achieve small area and comfortable wearing, dedicated OFDM transmission strategy, and on-chip oscillator (crystal-less) are introduced to the BCC system. Due to frequency offset of on-chip oscillator, the calibration methodology for crystal-less OFDM is included in the design.

This thesis presents a BCC emulation platform with dedicated OFDM transmission strategy and on-chip oscillator features. The emulation platform includes transmitter front-end, receiver front-end and transceiver baseband. It can achieve reliable transmission with 6.7Mbps data rate.

誌謝

在 Si2 實驗室的時間，是恕平在交大成長最快的一段時間。首先要感謝指導教授－李鎮宜博士，給予恕平在研究方向、方法以及態度的指導。李老師所建構出完善的研究環境以及強大研究團隊，讓恕平能夠在最好的環境跟最棒的團隊學習成長。除了在研究方面的指導外，李老師也時常鼓勵我們要養成運動的習慣。有健康的身體，做起事來效率才高。李老師做人做事的態度方法是我學習的榜樣。另外也要感謝口試委員黃威教授、莊景德教授以及周世傑教授，你們能撥空來指導並且給予我研究方面的建議，使得本篇論文可以更加完整。

特別感謝從專題時期就跟隨的偉豪學長。您在專業上的素養以及嚴謹的邏輯思考等，讓恕平十分佩服。四年多下來，恕平從您身上學到非常多的東西，受益良多。也感謝瑞元、燦文、盈杰、建螢、書餘以及秉原學長們，時常撥空給予我研究上的建議。感謝曉涵學姊以及子均學長在我專題時期，給予我的協助。感謝 Si2 的研究團隊們，你們的幫忙及鼓勵，是恕平突破及成長的動力。

感謝 Si2 的夥伴博堯，從比利時以來的陪伴。我們一同旅遊運動健身跑步，紓解研究上的壓力。感謝紝炘，在研究上的幫忙。讓我們一同合作，一起成長。感謝佩妤、姿儀、方如、英秀以及鈺筠，你們讓 Si2 的研究氣氛更為和樂融洽。最後感謝我的家人，因為你們的支持讓我可以順利的完成學位。

Table of Contents

Pages

List of Figures

List of Tables

Chapter 1:
Introduction

1-1 Introduction to BCC

Body channel communication (BCC) is an emerging technology which uses skin of human body as transmission channel. There are several advantages of body channel. First, Human body has high conductivity compared with air. Second, the transmission frequency of BCC is relatively low compared to other wireless communication. This removes the need for large antenna, and thus reduces the power consumption of system. Moreover, the transmission of signal is confined to the body area. These advantages make BCC suitable for following application scenario.

- Multimedia Download

Digital signage is getting more and more popular. However, how to take away information from digital signage still remains a hot issue. Existing communication technology such as Bluetooth and WiFi has high speed data-rate. However, users have to go through miscellaneous steps in order to download information. If we use BCC, when user touches digital signage, the channel between digital signage and mobile device is connected by body channel, and the information can be downloaded to the mobile devices. To download information within seconds, data rate is an important issue. The application scenario is shown in Fig. 1-1.

Fig. 1-1 Multimedia download

➢ Mobile Health-care Application

A typical mobile health-care system consists of multiple sensor nodes and one central processing node (CPN). The sensor nodes are usually small patch attach on human body, and monitor and collect bio-medical information such as ECG, EEG, EMG, and so forth. The collected bio-medical information is transmitted to CPN for further processes and analysis. Because sensor nodes are attached on human body, they should be comfortably wearing and have long usage duration. Because BCC transmission frequency is low, thus consumes lower RF power, which makes it very suitable to meet the demands. The application scenario is shown in Fig. 1-2.

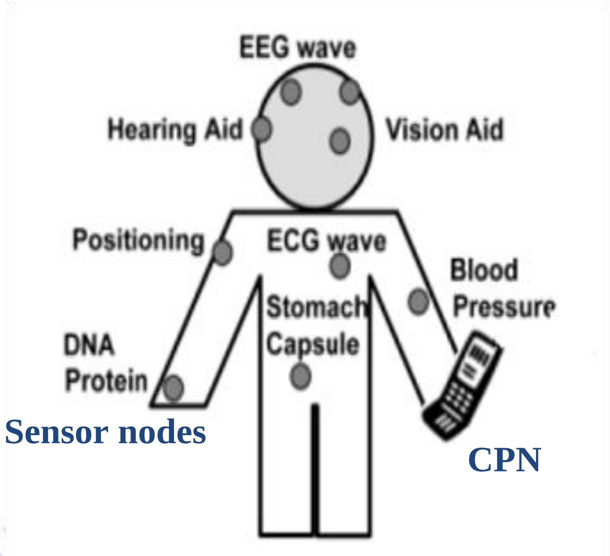

Fig. 1-2 Mobile health-care application

➢ Access Control and Payment

The purpose of access control is to open door or gate only when person who has specific identification shows up, and to block people who don't have such identification. Take gate control in Taipei MRT station for example, gate is open only when one has EasyCard(悠遊卡) and enough money in it. However, in everyday life, we can see that many people stand in front of gate, trying to find their EasyCard and let EasyCard very close to reader on the gate, thus blocking the gate and influencing the flow. Similar situation would happen when checking out in retail store such as 7-11, where people try to search for i-Cash card out of tens of different smart card (usually RFID).

If BCC comes into play, because transmission of signal is confined to the body area, BCC is very suitable for the application which needs trigger device only when person is near to that device, such as access control and payment application shown before. The application scenario is shown in Fig. 1-3, we turn the RFID smart cards (EasyCard, i-Cash...) into App in mobile devices, such as smart phone and tablet. When user touches reader, BCC then connect reader and mobile devices. Mobile devices could be in packet, backpack, where it is near body area.

Fig. 1-3 Access control and payment

1-2 Motivation and Design Approach

From BCC application scenarios, we can find out that energy efficiency, area, and high data-rate are important design issues. There have been some studies to BCC, paper [1] uses PPM, [2], [3] use FSK modulation, and [4] uses PAM. In low data-rate transmission, it requires longer operation duration, thus dissipates higher overall energy. Besides, in paper[2], it estimates the channel condition first, and then chooses the suitable channel for transmission. This is somehow complicate, and will limit the data rate. Paper [5] uses frequency hopping to combat the channel effect. However, it occupies pretty large bandwidth (80MHz). When it comes to issue of area and comfort of wearing, papers[2], [4] and [5] use external clock source. The external clock source usually is quartz crystal, which is large and bulky.

This thesis proposes a crystal-less OFDM system for BCC applications. With dedicated OFDM transmission strategy, high data rate and energy efficiency is achieved. For comfortable wearing, we use on-chip oscillator integration (crystal-less) to replace large and bulky quartz crystal. On-chip oscillator has supreme excess compared with quartz crystal oscillator in terms of area and process integration[6]. However, the frequency offset of the on-chip oscillator is larger than the tolerance of conventional packet-based OFDM system, thus a dedicated clock calibration methodology is included in the system.

1-3 Organization

The thesis is organized as follows. Chapter 2 is the overview of the proposed system, which describes body channel characteristics and crystal-less issues. The design of proposed BCC transceiver is shown in Chapter 3. The BCC emulation platform implementation is shown in Chapter 4. The experiment result is sown in Chapter 5. Finally, Chapter 6 gives the conclusion and future work.

Chapter 2:
Overview of BCC and Crystal-less Integration

2-1 Body Channel Characteristics

2-1.1 Transfer Type

There are two ways which signal could transduce from transceiver to the human body, as shown in Fig. 2-1. One is Galvanic transfer, which attach electrode directly to human skin. Another is capacitive coupling. Galvanic transfer is generally considered as the most efficient way to transducer signal, however, there are still some concerns about the potential risk of directly induce current from electrodes to human skin. Instead of directly attaching electrodes to human skin, capacitive coupling method transduces signal through generating electromagnetic wave from electrodes, and this electromagnetic wave induces signal on human skin.

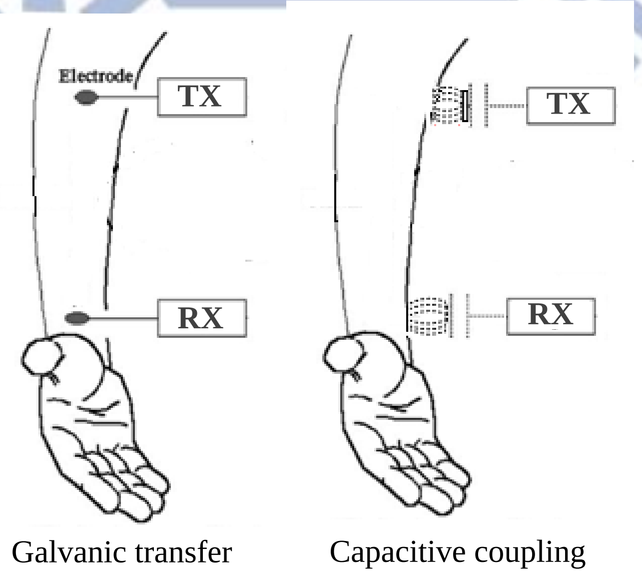

Fig. 2-1 BCC Coupling types

2-1.2 Types of Transmission

There are three types of transmission for BCC [7], as shown in Fig. 2-2, which are simple circuit type, electrostatic coupling type, and waveguide type.

The simple circuit type treats human body simply as conductor. Although it is a simple transmission method, it needs additional wire to connect TX and RX. Fat meter belong to this type. However, this type of transmission is not suitable for our application.

Second type is electrostatic coupling. In this type of transmission, TX and RX are capacitive coupling to earth ground, thus don't need additional wire. However, the transmission quality is influenced by the surrounding subjects.

Third type regards human body as waveguide, and electromagnet wave is generated by differential nodes, which propagates from TX to RX. This type of transmission is less influenced by individual's surroundings.

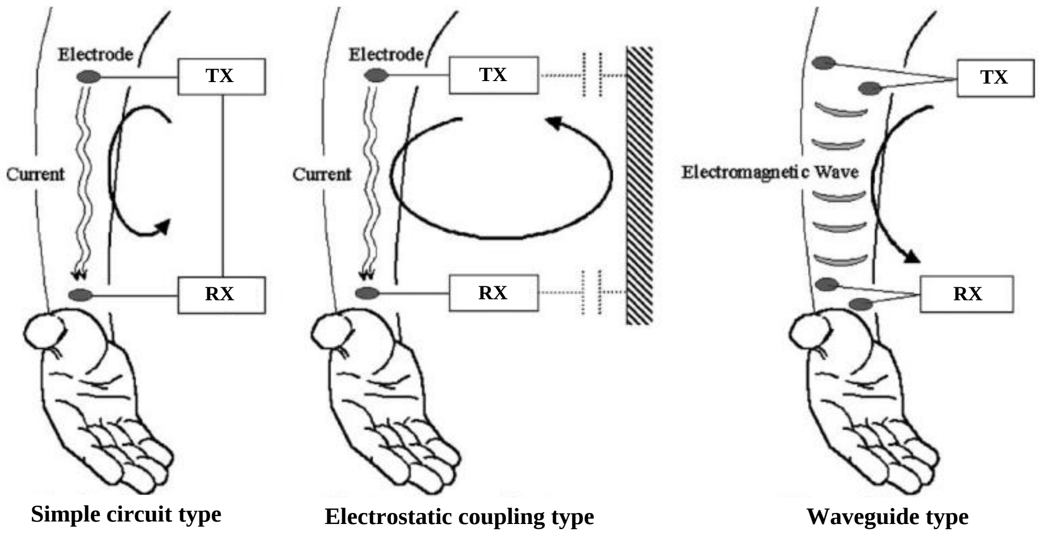

Fig. 2-2 BCC transmission types

2-1.3 Path-loss

The path-loss of body channel changes with frequency and position of two electrodes. Fig. 2-3 shows the measurement set-up. Function generator transmits specific power with different frequencies, and we get received power from the spectrum analyzer. The difference between the power is the channel path-loss.

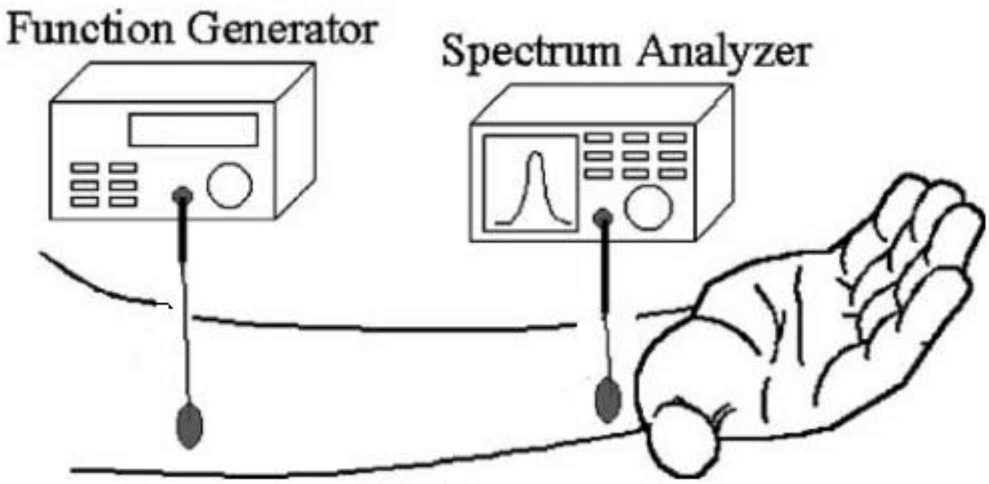

Fig. 2-3 Measurement set-up

Fig. 2-4 shows the frequency response of body channe. From the figure, we can see that path between 10MHz to 40MHz is rather flat. Thus this band is suitable for signal transmission. Table 2-1 is the path-loss with different electrode positions, and either electrodes are attached to skin (Galvanic transfer) or not (capacitive coupling).

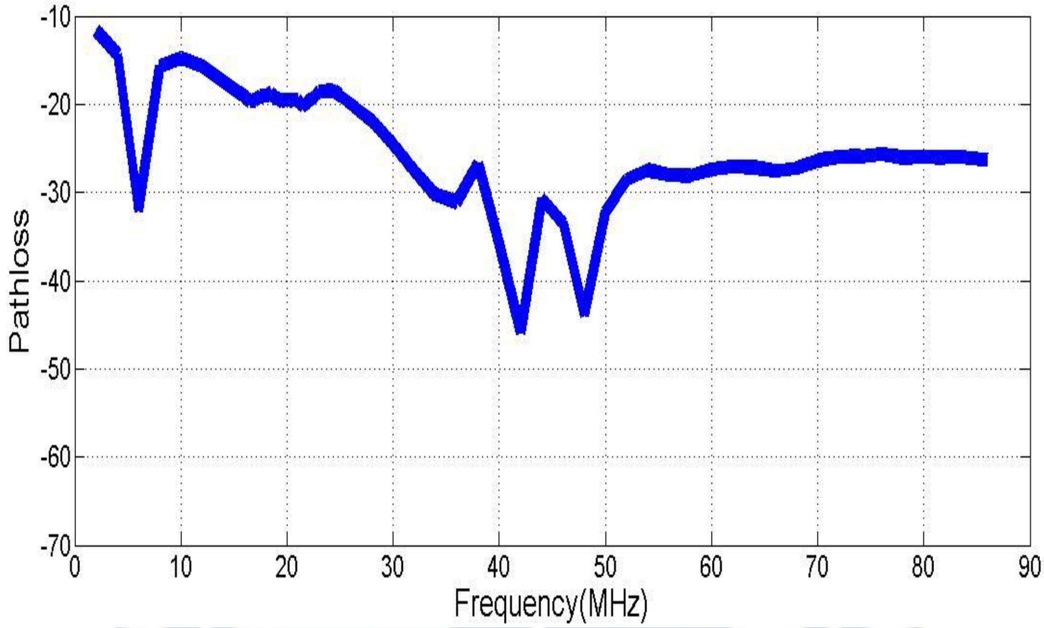

Fig. 2-4 Frequency response

Table 2-1 Path-loss measurement

Electrode Positions	**Path-loss (dB)** (Galvanic transfer / 1mm apart Capacitive coupling)
1	18.19 / 18.39
2	19.09 / 20.69
3	23.89 / 24.89
4	24.89 / 26.89
5	26.89 / 29.89
6	27.89 / 31.89

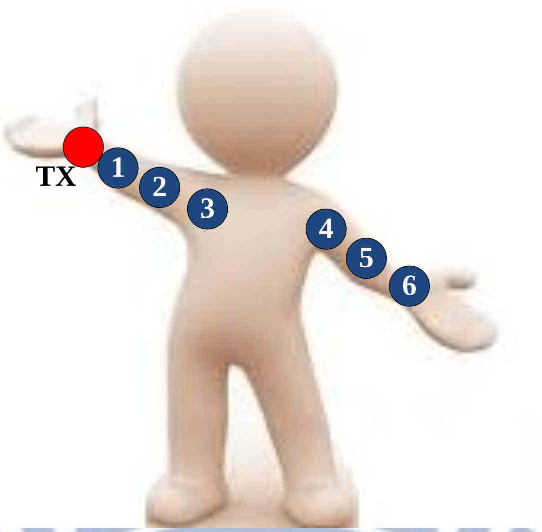

2-1.4 Body Antenna Effect

Human body is a lossy conductor with complex shape, thus it can be considered as wideband antenna [2], which is called body antenna effect. Since human body acts as a wideband antenna, it picks up surrounding radio signal, which degrades signal to interference ratio (SIR) in transmission. To measure the body antenna effect, the measurement set-up and result is shown in Fig. 2-5. Solid line is measure when electrode is not attached on human skin (a), dashed line is when electrode is attached on human skin (b). From the measurement, the maximum is about 28dB.

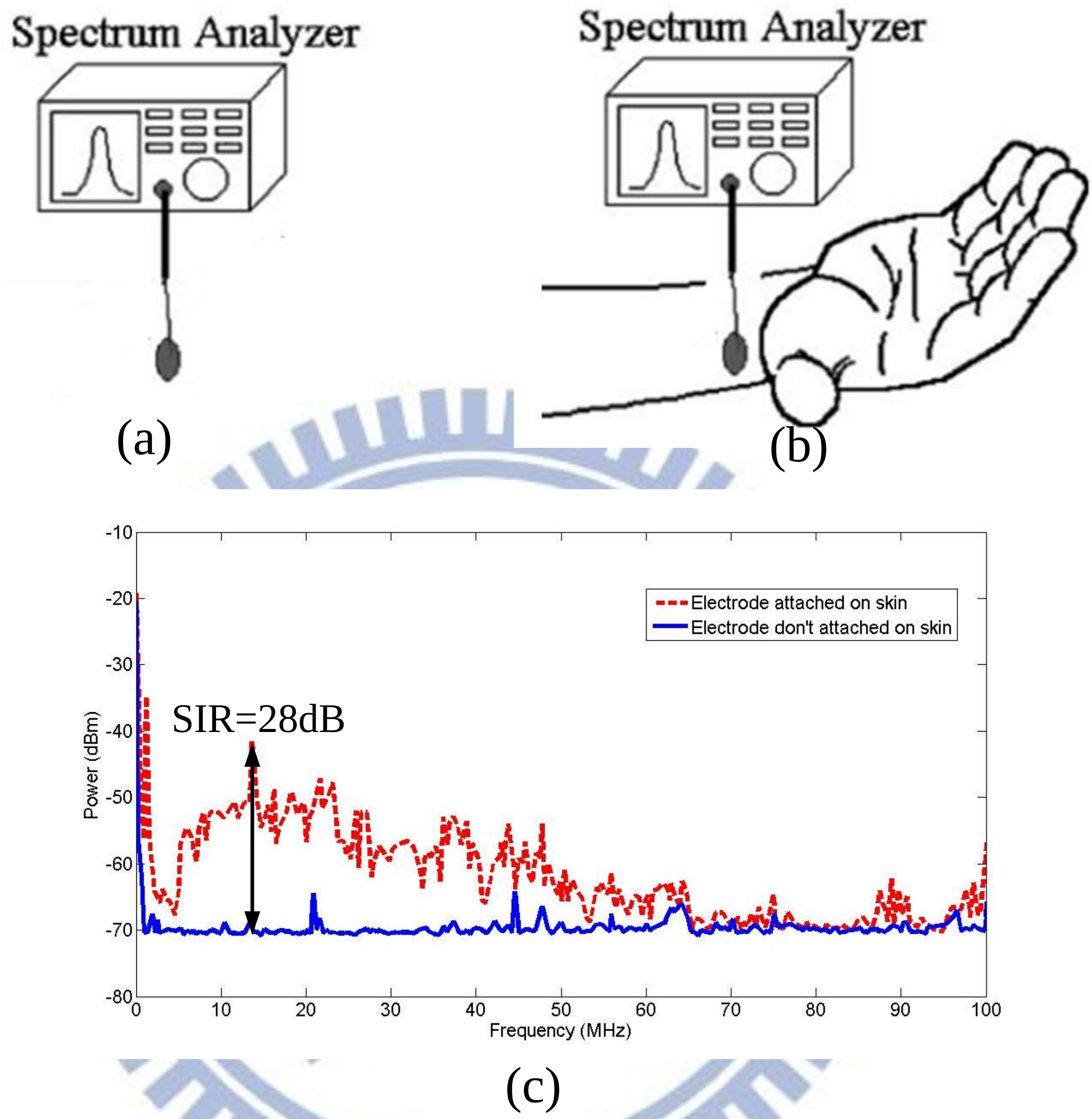

Fig. 2-5 Interference measurement

2-1.5 Body Channel Model

In document IEEE P802.15-08-0780-06-0006, it describes the scenarios for body area network, as shown in Fig. 2-6. Based on placement of communication nodes and transmission frequency, Table 2-2 lists all the scenario. From Fig. 2-6 and Table 2-2, we can find out that our proposed BCC falls into scenario S4 and S5, body surface to body surface, which belongs to channel model CM3.

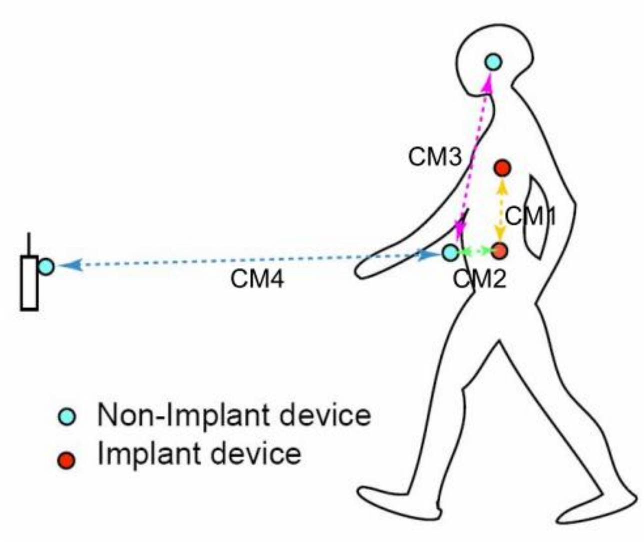

Fig. 2-6 Body area network scenario

Table 2-2 Body area network scenario

Scenario	Description	Frequency Band	Channel Model
S1	Implant to Implant	402-405 MHz	CM1
S2	Implant to Body Surface	402-405 MHz	CM2
S3	Implant to External	402-405 MHz	CM2
S4	Body Surface to Body Surface (LOS)	13.5, 50, 400, 600, 900 MHz 2.4, 3.1-10.6 GHZ	CM3
S5	Body Surface to Body Surface (NLOS)	13.5, 50, 400, 600, 900 MHz 2.4, 3.1-10.6 GHZ	CM3
S6	Body Surface to External (LOS)	900 MHz 2.4, 3.1-10.6 GHZ	CM4
S7	Body Surface to External (NLOS)	900 MHz 2.4, 3.1-10.6 GHZ	CM4

The channel model from IEEE P802.15-08-0577-01-0006 is composed of frequency response and noise characteristics, as shown in Fig. 2-7. The measurement result of frequency response is shown in Fig. 2-8, and noise characteristic is shown in Fig. 2-9. The mean is zero and variance is 2.55×10^{-5} and can be fitted into Gaussian distribution. The block diagram for channel model is shown in Fig. 2-10. Channel filter is the human body frequency response, which is valid between 0MHz to 50MHz, and the channel noise is the EM waves generated by electronic devices which couple into human body due to body antenna effect.

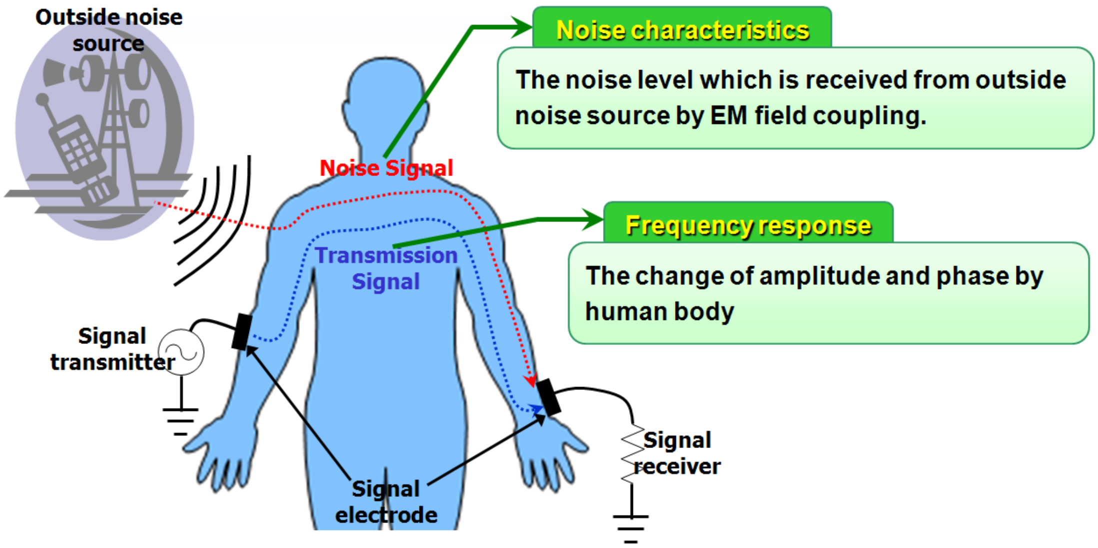

Fig. 2-7 Body channel model

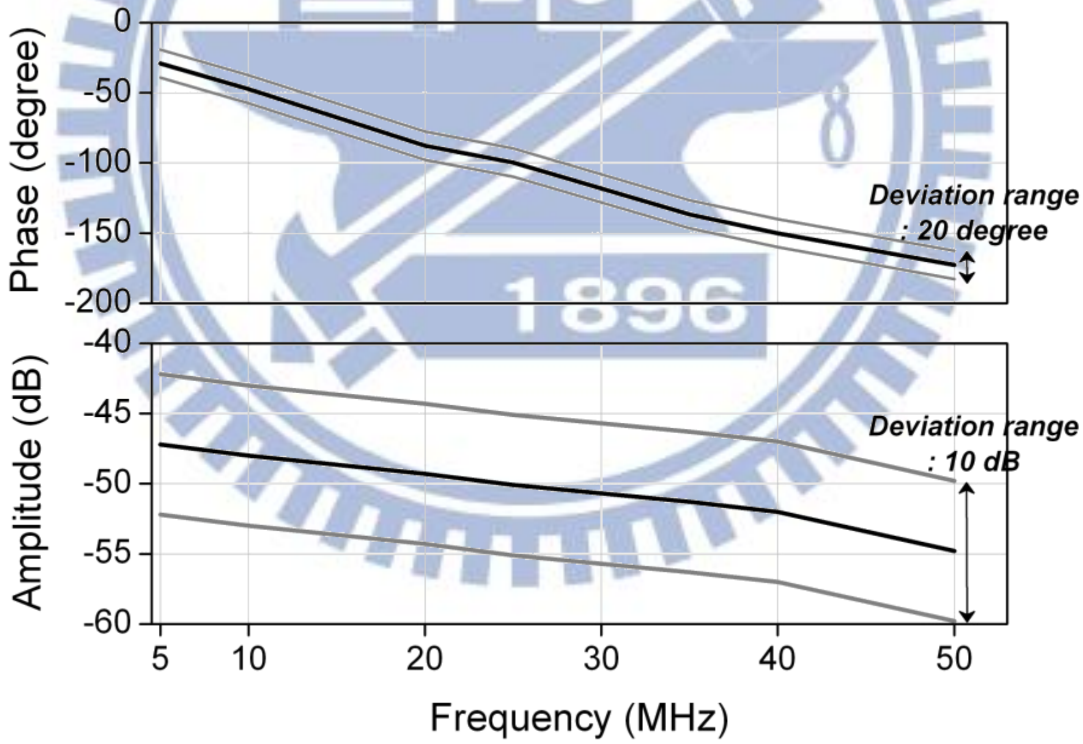

Fig. 2-8 Frequency response

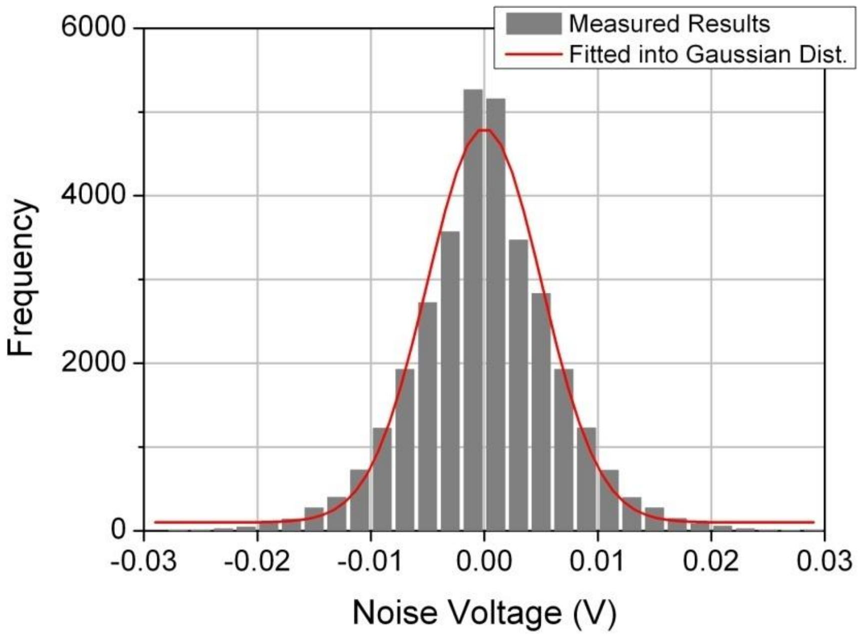

Fig. 2-9 Noise characteristic

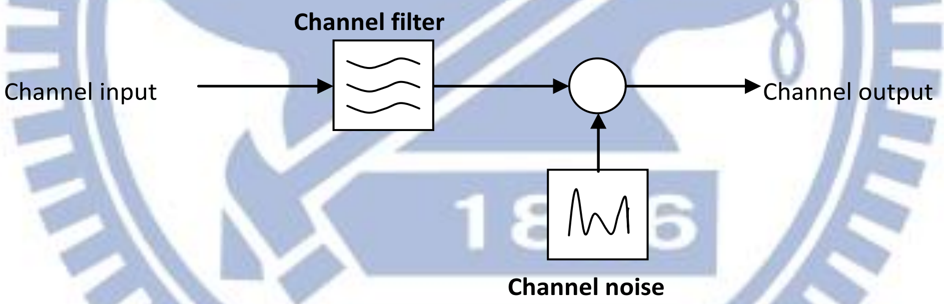

Fig. 2-10 Channel model block diagram

The mathematical expression is shown in Equation $h(t)=h_R(t)\cdot C_h$

(2-1). where $h_R(t)$ is the channel impulse response and C_h is a coefficient related to sizes of ground planes and distances between Tx and Rx.

$$h(t)=h_R(t)\cdot C_h \tag{2-1}$$

where

$$h_R(t) = A_V \cdot A \cdot \exp(-(t - t_r)/t_0) \cdot \sin(\pi \cdot (t - t_r - x_c)/w)$$

A_v represents the fluctuation of path-loss. It can be described by Gaussian distribution.

$A_v \sim N(1, 0.16^2)$

The A, t_r, t_0, x_c and w has constant values as follows:

Time range (μs)	A	t_r	t_0	x_c	w
$0 \le t < 0.025$	0.00032	0.00000	0.00621	-0.00097	0.00735
$0.025 \le t < 0.058$	0.00003	0.02500	0.01684	-0.01225	0.00944
$0.058 \le t$	0.00002	0.05800	0.05610	0.00100	0.01109

$$C_h = (0.0422 \cdot G_T - 0.184) \cdot (0.0078 \cdot G_R + 0.782) \cdot \left(\frac{120.49}{d_{body} + d_{body} \cdot (d_{air} / d_{body})^5} \right)^2$$

G_T and G_R are the ground plane's size(cm^2) for TX and RX

d_{air} and d_{body} are transmission distance through air and body.

The valid range are : $10cm^2 \le G_T, G_R \le 270\ cm^2$, $10\ cm \le d_{air}, d_{body} \le 200\ cm$

Following shows the matlab simulation with $G_T = G_R = 15\ cm^2$ under different conditions. Fig. 2-11 is when $d_{air} = d_{body} = 10cm$, Fig. 2-12 is when $d_{air} = d_{body} = 30cm$, and Fig. 2-13 is when $d_{air} = 100cm$, $d_{body} = 150cm$.

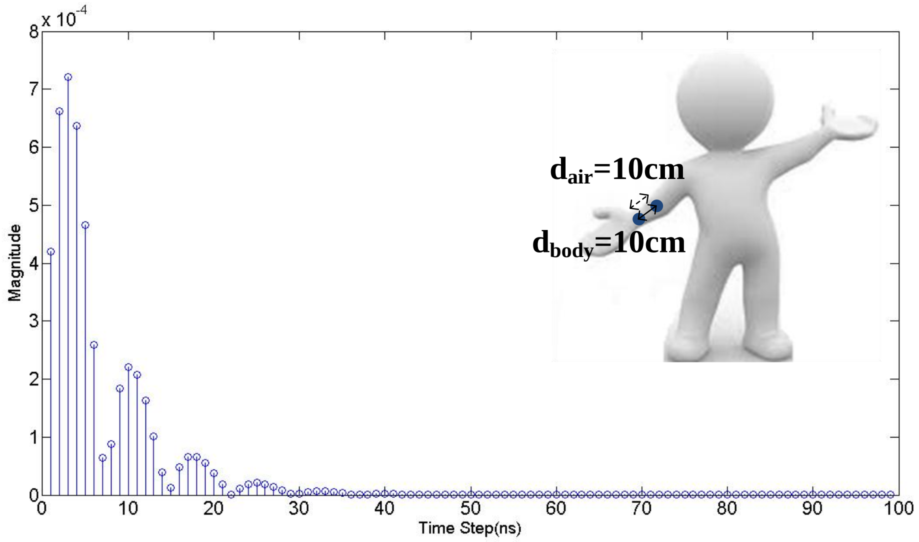

Fig. 2-11 Channel with d_{air} = d_{body} = 10cm

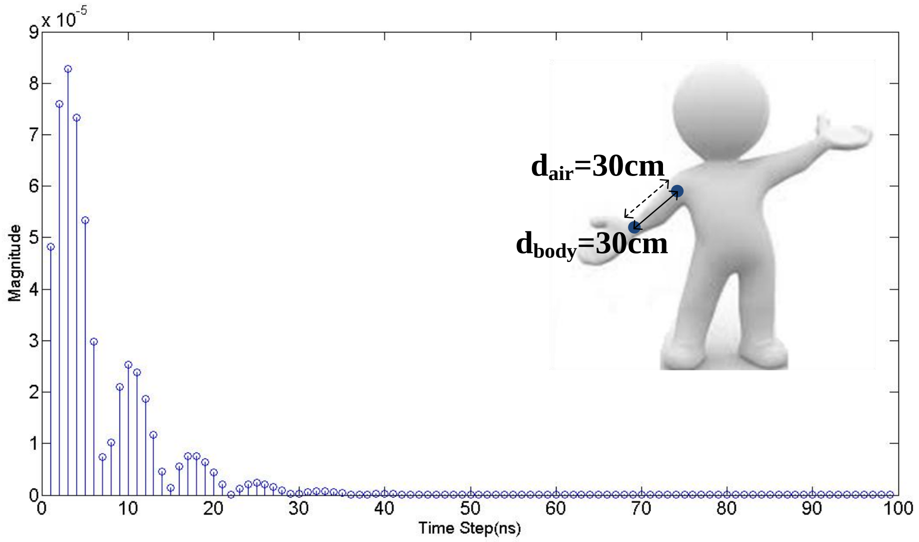

Fig. 2-12 Channel with d_{air} = d_{body} = 30cm

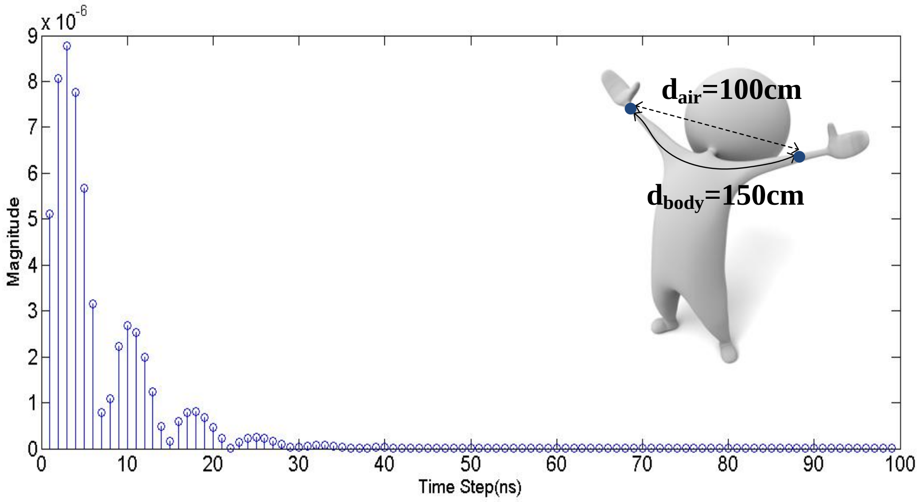

Fig. 2-13 Channel with d_{air} =100cm, d_{body} = 150cm

2-2 Crystal-less Integration Issues

2-2.1 Crystal-less Integration Overview

In Mobile Health-care application, for comfortable wearing of sensor nodes, we use on-chip oscillator integration (crystal-less) to replace large and bulky quartz crystal, as shown in Fig. 2-14. On-chip oscillator has supreme excess compared with quartz crystal oscillator in terms of area and process integration[6]. However, the frequency offset of the on-chip oscillator is larger than the tolerance of conventional packet-based OFDM system. This frequency offset of the on-chip oscillator causes carrier frequency offset (CFO) and sampling clock offset (SCO) in the system, as shown in Fig. 2-15.

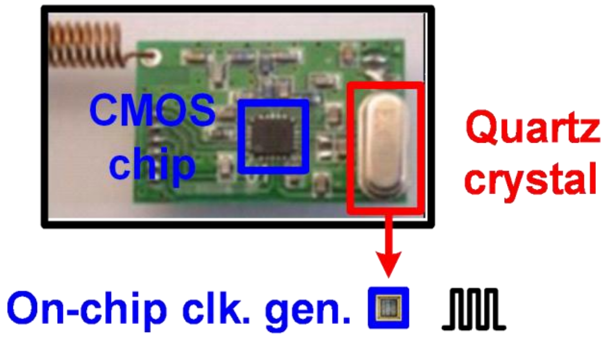

Fig. 2-14 On-chip oscillator integration

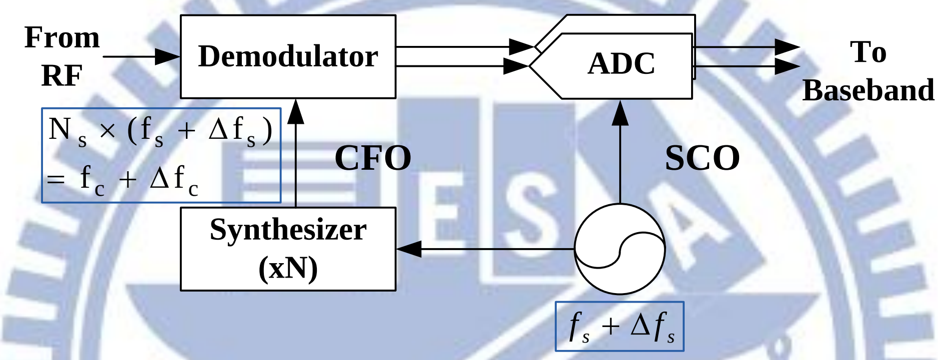

Fig. 2-15 CFO and SCO effect

2-2.2 Carrier Frequency Offset

From Fig. 2-15 we can see that CFO in our system is mainly caused by frequency offset of on-chip oscillator. Assume accurate clock frequency is f_s , and frequency offset of on-chip oscillator is Δf_s. Δf_s goes through synthesizer and multiply by N, which becomes $\Delta f_C = N_S \Delta f_S$. The mathematical expression of received CFO signal is shown in equation(2-2). $z(t)$ is the received signal from RF, N is number of carrier, and Ng is number of cyclic prefix.

$$z_{i,n} = z(t)e^{j2\pi\Delta f_C t}\big|_{t=i(N+N_g)T_S+N_gT_S+nT_S} \qquad (2\text{-}2)$$

Frequency domain expression is equation(2-3)

$$Z_{i,k} = X_{i,k-\varepsilon_{Il}} H_{k-\varepsilon_I} \frac{\sin(\pi\varepsilon_f)}{N\sin(\frac{\pi\varepsilon_f}{N})} e^{j2\pi\frac{i(N+N_g)+N_g}{N}(\varepsilon_I+\varepsilon_f)} e^{j\pi\frac{N-1}{N}\varepsilon_f}$$
$$+\sum_{l=-N/2+l,\, l\neq k-\varepsilon_l}^{N/2} X_{i,l} H_l \frac{\sin(\pi(\varepsilon_l+\varepsilon_f+l-k))}{N\sin(\frac{\pi(\varepsilon_I+\varepsilon_f+l-k)}{N})} e^{j2\pi\frac{i(N+N_g)+N_g}{N}(\varepsilon_I+\varepsilon_f)} e^{j\pi\frac{N-1}{N}(\varepsilon_I+\varepsilon_f+l-k)} \qquad (2\text{-}3)$$
$$+V_{i,k}$$

We can express carrier frequency as $\Delta f_c = (\varepsilon_I + \varepsilon_f)\frac{1}{NT_s}$, where ε_I is integer frequency offset, and ε_f is fractional frequency offset, $0.5 \le \varepsilon_f \le 0.5$

$$Z_{i,k} = X_{i,k-\varepsilon_{Il}} H_{k-\varepsilon_I} \frac{\sin(\pi\varepsilon_f)}{N\sin(\frac{\pi\varepsilon_f}{N})} e^{j2\pi\frac{i(N+N_g)+N_g}{N}(\varepsilon_I+\varepsilon_f)} e^{j\pi\frac{N-1}{N}\varepsilon_f}$$
$$+\sum_{l=-N/2+l,\, l\neq k-\varepsilon_l}^{N/2} X_{i,l} H_l \frac{\sin(\pi(\varepsilon_l+\varepsilon_f+l-k))}{N\sin(\frac{\pi(\varepsilon_I+\varepsilon_f+l-k)}{N})} e^{j2\pi\frac{i(N+N_g)+N_g}{N}(\varepsilon_I+\varepsilon_f)} e^{j\pi\frac{N-1}{N}(\varepsilon_I+\varepsilon_f+l-k)}$$
$$+V_{i,k}$$

From equation(2.3) we can find out that ε_I causes index shift as well as phase rotation. ε_f causes magnitude attenuation, phase rotation, and ICI(second term in equation). $V_{i,k}$ is the channel noise component.

2-2.3 Sampling Clock Offset

Sampling clock offset (SCO) happens when clock frequency of TX DAC and clock frequency of RX ADC are different. In our system, there is one accurate quartz crystal clock at CPN, and inaccurate on-chip oscillator at sensor nodes. Assume quartz crystal clock period equals to T_s, and on-chip oscillator clock period equals to $(1+\delta)T_s$, then we can express n-th received sample of i-th symbol as equation(2-4)

$$z_{i,n} = z(t)\big|_{t=i(N+N_g)(1+\delta)T_S + N_g(1+\delta)T_S + n(1+\delta)T_S} \tag{2-4}$$

The frequency domain expression is equation(2.5)

$$\begin{aligned} Z_{i,k} &= X_{i,k}H_k \frac{\sin(\pi\delta k)}{N\sin(\frac{\pi\delta k}{N})} e^{j2\pi\frac{i(N+N_g)+N_g}{N}\delta k} e^{j\pi\frac{N-1}{N}\delta k} \\ &+ \sum_{l=-N/2+1,\, l\neq k}^{N/2} X_{i,l}H_l \frac{\sin(\pi((1+\delta)l-k))}{N\sin(\frac{\pi((1+\delta)l-k)}{N})} e^{j2\pi\frac{i(N+N_g)+N_g}{N}\delta l} e^{j\pi\frac{N-1}{N}[(1+\delta)l-k]} + V_{i,k} \end{aligned} \tag{2-5}$$

From the first term of equation

$$\begin{aligned} Z_{i,k} &= X_{i,k}H_k \frac{\sin(\pi\delta k)}{N\sin(\frac{\pi\delta k}{N})} e^{j2\pi\frac{i(N+N_g)+N_g}{N}\delta k} e^{j\pi\frac{N-1}{N}\delta k} \\ &+ \sum_{l=-N/2+1,\, l\neq k}^{N/2} X_{i,l}H_l \frac{\sin(\pi((1+\delta)l-k))}{N\sin(\frac{\pi((1+\delta)l-k)}{N})} e^{j2\pi\frac{i(N+N_g)+N_g}{N}\delta l} e^{j\pi\frac{N-1}{N}[(1+\delta)l-k]} + V_{i,k} \end{aligned}$$

(2-5), we can see clock offset δ causes magnitude attenuation and phase rotation. Phase rotation is proportional to k and index i, which means phase rotation becomes larger at later symbol. Second term is inter-carrier interference. $V_{i,k}$ is the channel noise component.

Chapter 3: Design of Crystal-less OFDM-based Transceiver Baseband

3-1 OFDM Transmission Strategy

OFDM has been a very popular modulation for high data-rate transmission. Moreover, we further take the high data-rate advantage of OFDM to reduce the overall transmission energy. From Fig. 3-1, we can explore the low energy strategy behind packet-based OFDM. When in sleep mode, only the storage component of the system operates, and other blocks are turned into sleep mode (power gated). While the data is collected to certain amount, system turns into active mode, and transmit the data in one shot. Therefore it uses high data-rate transmission ability of OFDM to reduce the operation time of transmission blocks, thus reducing the overall operation energy. Mathematical analysis is shown in Equation

$$
\begin{aligned}
E_{sample} &= \frac{P_{on}T_{on} + (P_{off} + P_{storage})T_{cycle}}{M} \\
&= \frac{P_{on}(T_{setup} + T_p + N \times M / f_d) + (P_{off} + P_{storage})(M / f_s)}{M} \\
&= \frac{P_{on}(T_{setup} + T_p)}{M} + \frac{N \times P_{on}}{f_d} + \frac{P_{off} + P_{storage}}{f_s}
\end{aligned}
\qquad (3\text{-}1)
$$

Assume storage component can store M samples each contains N bits.

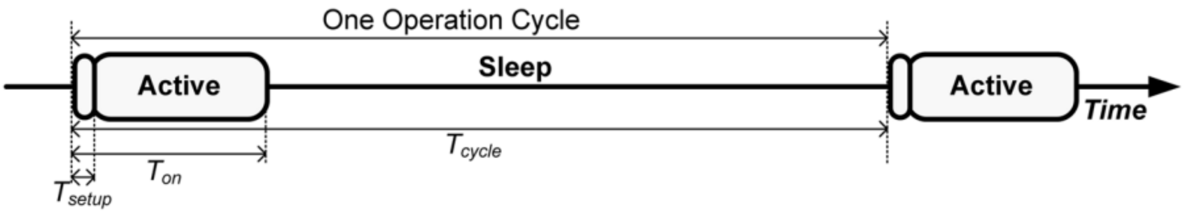

Fig. 3-1 OFDM transmission strategy

$$
\begin{aligned}
E_{sample} &= \frac{P_{on}T_{on} + (P_{off} + P_{storage})T_{cycle}}{M} \\
&= \frac{P_{on}(T_{setup} + T_p + N \times M / f_d) + (P_{off} + P_{storage})(M / f_s)}{M} \\
&= \frac{P_{on}(T_{setup} + T_p)}{M} + \frac{N \times P_{on}}{f_d} + \frac{P_{off} + P_{storage}}{f_s}
\end{aligned}
\tag{3-1}
$$

where

P_{on} : System dynamic power (Exclude storage component)

P_{off} : System leakage power (Exclude storage component)

$P_{storage}$: Storage component power

f_s : Sampling rate of data collecting

f_d : Transmission rate

T_{cycle} : Duration need fulfill storage component

T_{on} : System active duration

T_{setup} : Setup time from sleep to active

T_p : Preamble transmission time

3-2 OFDM Packet Format

Fig. 3-2 is packet format of our system. It is combination of 10 identical short preambles (Fig. 3-3), which is used for synchronization and clock calibration. GI2 is the last 32 points of long preamble, we uses GI2 for boundary detection. Following is 2 identical long preambles(Fig. 3-4) which are used for channel estimation and fine-CFO estimation. Two SIG packets show the size of payload. Finally is the payload which contains the data.

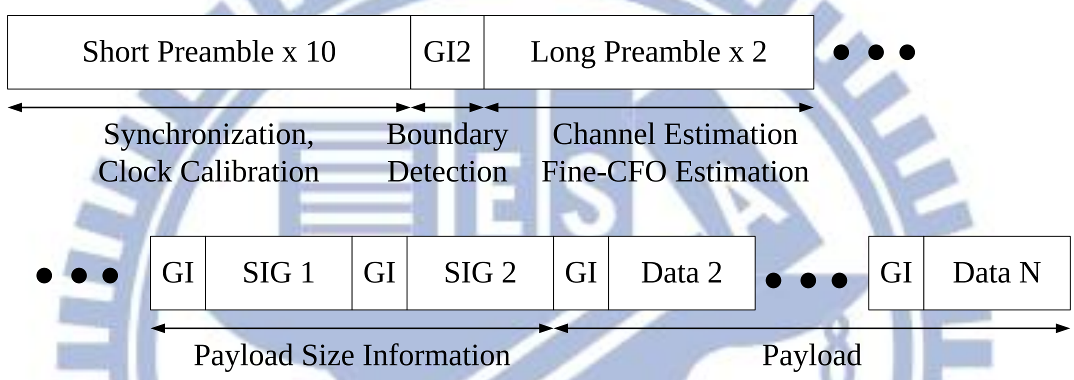

Fig. 3-2 Packet Format

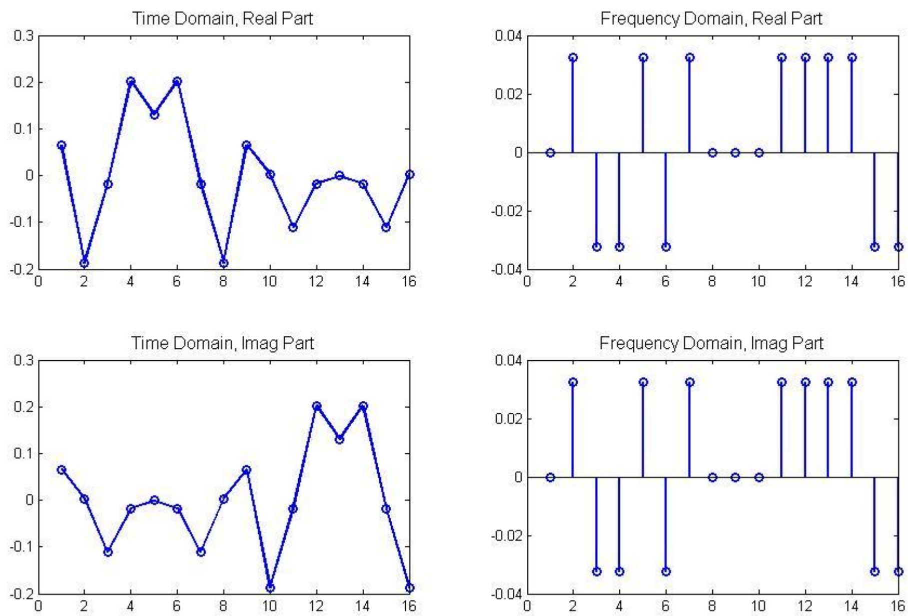

Fig. 3-3 Short Preamble

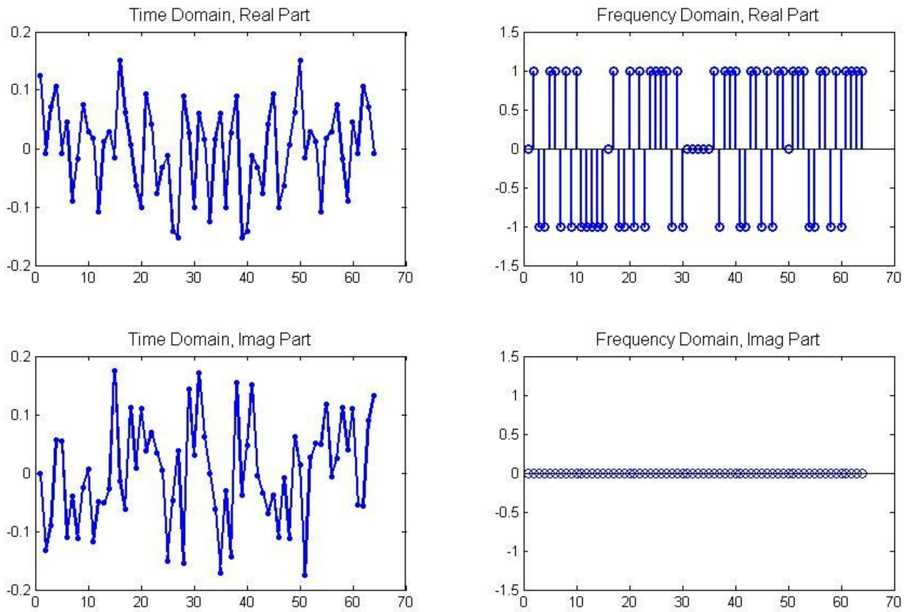

Fig. 3-4 Long Preamble

3-3 Proposed Crystal-less OFDM-based Transceiver Baseband

3-3.1 Baseband Overview

Fig. 3-5 shows the proposed BCC transceiver baseband. At TX baseband, mapper maps bitstream into QPSK symbol. Then IFFT transfer symbol from frequency domain to time domain. In time domain, CP is added in front of each symbol. Finally the preamble and SIG are added at beginning of the packet.

At RX baseband, after packet is detected, AGC calculates the power and sends the codeword to DVGA to tune the gain of it, and CLK drift estimator estimates the clock offset and sends the corresponding codeword to on-chip oscillator to tune the frequency. After the clock is calibrated, packet goes through boundary detection, which uses dual-correlation algorithm.

After boundary is detected, the following payload transform to frequency domain. In frequency domain, it further does post-FFT compensation before de-mapping QPSK into bit-stream.

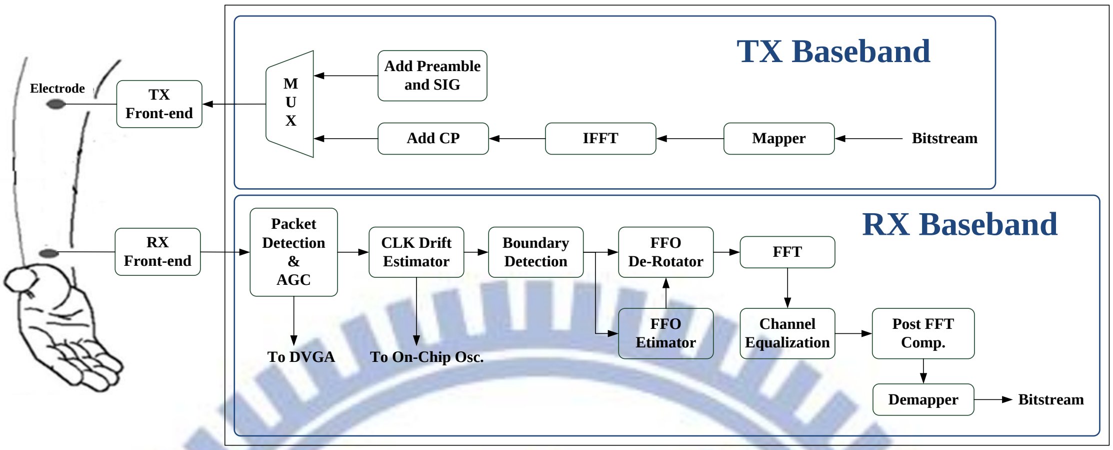

Fig. 3-5 Transceiver Baseband Block Diagram

3-3.2 Synchronization and Clock Calibration

- Detection

Equation (3-2) shows the algorithm for packet detection. The basic idea behind algorithm is auto-correlation. In our design, we aim to detect the coming of two repetitive short preambles, so R = 16, L = 16. The short preamble is designed to be pseudo-noise, so the peak shows up when two symbols are the same. Fig. 3-6, shows the waveform when short preamble shows up. In our packet format, there are 10 repetitive short preambles, so the waveform looks like plateau when short preamble comes in. The packet is detected when auto-correlation is larger than pre-defined threshold, as shown in Fig. 3-6.

$$\phi(m) = \left| \sum_{r=0}^{R-1} z_{m-r} z_{m-r-L}^{*} \right| \qquad (3\text{-}2)$$

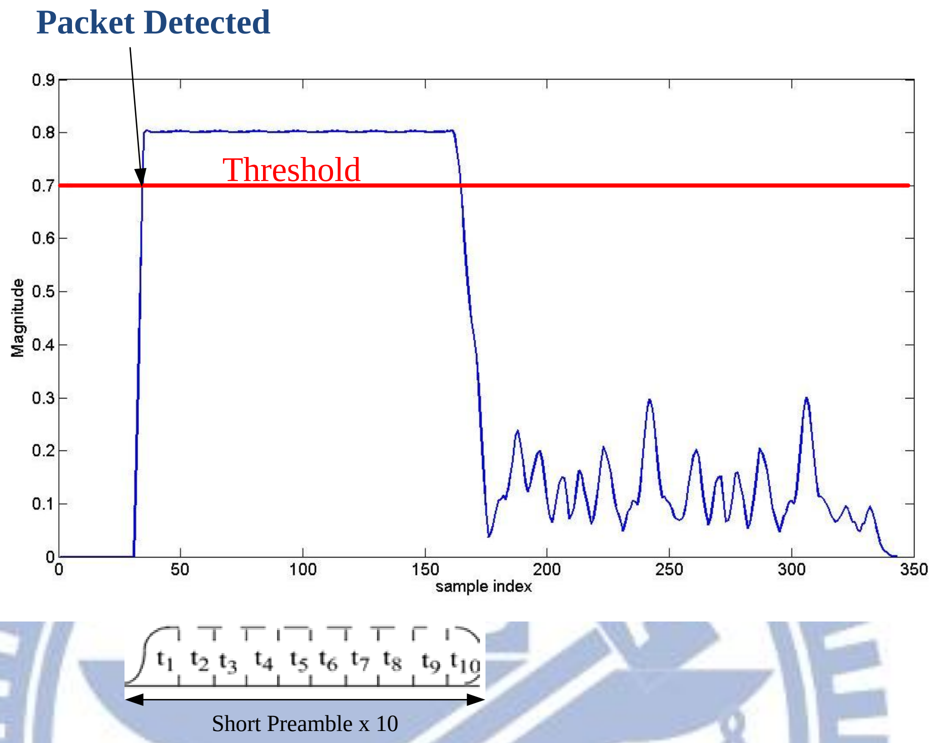

Fig. 3-6 Auto-correlation Waveform

- Auto Gain Control

As described in chapter 2-1.3, path-loss of body channel changes as transmission types (Galvanic transfer or capacitive coupling), different position of electrodes, and transmission frequency. Thus Auto Gain Control (AGC) is needed in order to remain swing of input signal, which will influence BER performance of system. Equation(3-3) shows the equation for AGC. When packet is detected, AGC compare the input signal power with ideal signal power, thus calculating the needed gain. Then AGC converts the gain into corresponding codeword to tune digital variable gain amplifier (DVGA). Fig. 3-7 is the flow chart of AGC.

$$Gain_{\phi(m)>Threshold} = \frac{\left|\sum_{r=0}^{R-1} z_{m-r} z^{*}_{m-r-L}\right|}{\left|\sum_{r=0}^{R-1} x_{m-r} x^{*}_{m-r-L}\right|} \quad (3\text{-}3)$$

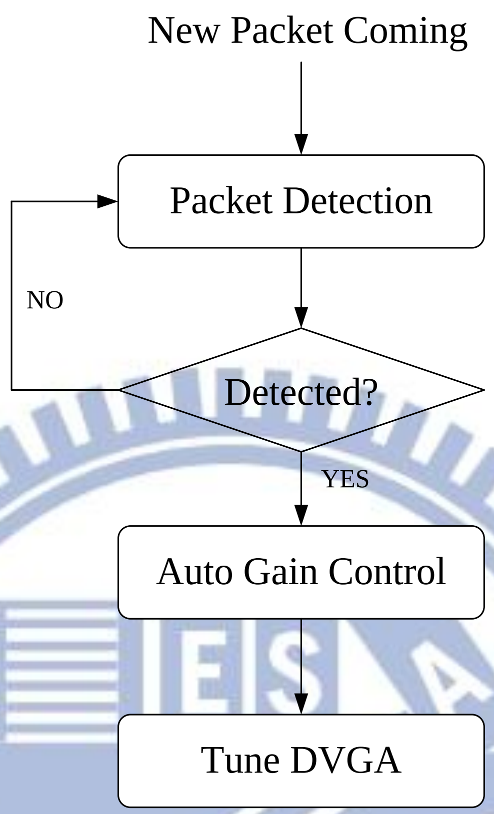

Fig. 3-7 AGC Flow Chart

- Clock Drift Estimator

When there is frequency offset in the oscillator, it will cause sampling clock offset (SCO), and then go through synthesizer, and become carrier frequency offset (CFO). Thus we can extract oscillator frequency offset from CFO, and then send corresponding codeword to tune the oscillator. Fig. 3-8 is the block diagram for clock drift estimator. After packet detection and AGC, estimator Ⅰ uses the short preambles to calculate the fractional frequency offset. Then de-rotator rotates the short preambles phase due to value from estimator Ⅰ. After de-rotation, short preamble comes into estimator Ⅱ. Total frequency offset equals to combination of value calculated by estimator Ⅰ and estimator Ⅱ. Then DDFS tuning codeword mapping maps the calculated frequency offset to corresponding DDFS codeword.

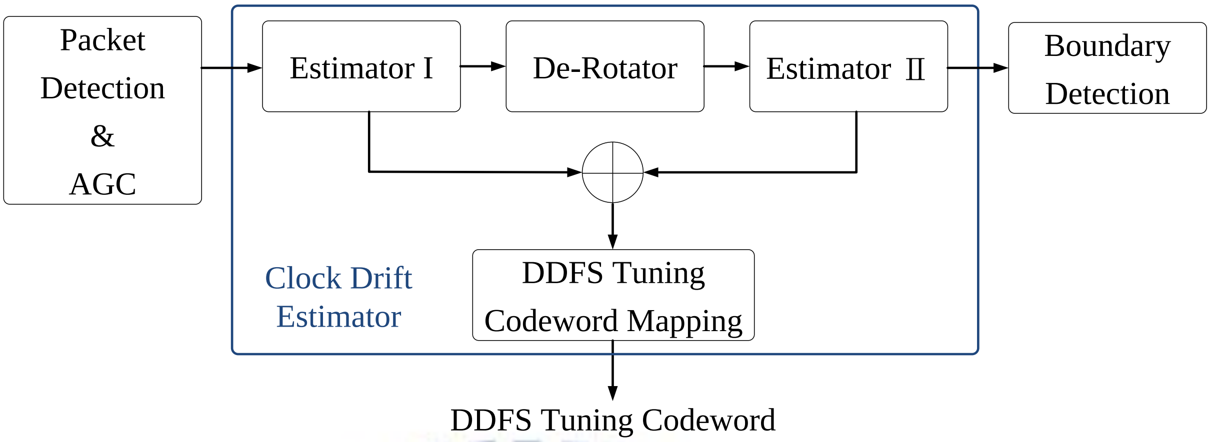

Fig. 3-8 Clock Drift Estimator

- Estimator I

Here we use maximum likelihood estimation to calculate CFO, as shown in Equation(3.5). Z_m in the equation is the short preamble.

Fig. 3-9 is the estimation offset when clock offset equals 4000ppm. It shows that estimation value oscillates around real offset value, thus we take the mean of estimation value over a sequence. The overall clock offset is shown in Equation(3-4).

Phase can only resolve in range of $\pm\pi$, which corresponds to ideal estimation range equals to $\pm 1/2LT_S$. Since the baseband data also suffer from SCO, the actual estimation range will smaller than $\pm 1/2LT_S$. From Matlab simulation (Fig. 3-9), when T_S is 5MHz, the toleration of algorithm is $\pm$4000ppm.

$$z_{i,n} = z(t)e^{j2\pi\Delta f_c t}\Big|_{t=i(N+N_g)T_s+N_gT_s+nT_s} \qquad (3\text{-}4)$$

$$\Delta\hat{f}c = \frac{1}{N}\,\mathrm{avg}\{\frac{1}{2\pi LT_s}\angle(\sum_{r=0}^{R-1} z_{m-r}z^{*}_{m-r-L})\} \qquad (3.5)$$

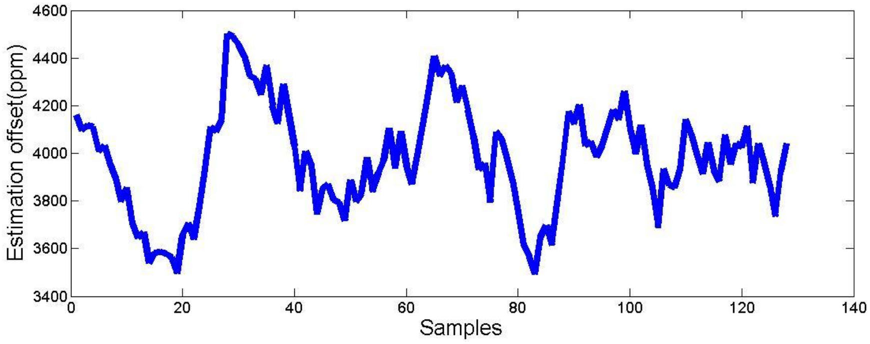

(a)

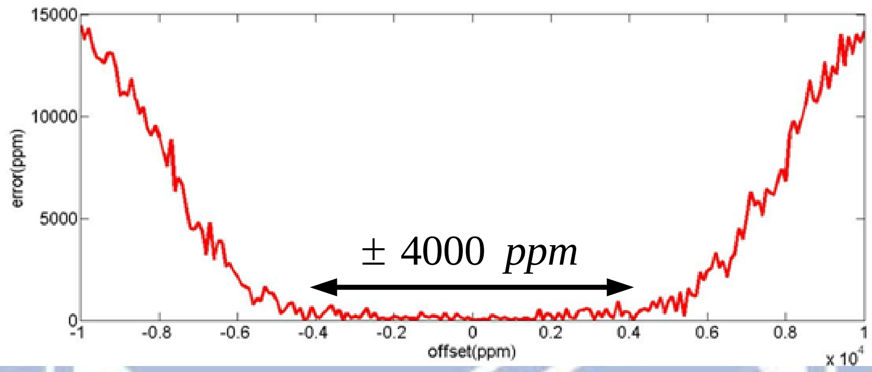

(b)

Fig. 3-9 Matlab simulation of clock drift estimation

- Estimator Ⅱ

We use Estimator Ⅱ to estimator larger frequency offset. Estimator Ⅱ uses match filter approach to detect the specific frequency offset. As shown in Fig. 3-10 and Equation(3-5)

H_0: $x[n] = s_0[n] + w[n]$

H_i : $x[n] = s_i[n] + w[n]$

$\vdots$

H_k: $x[n] = s_k[n] + w[n]$ (3-6)

where

$s_i[n]$:Detector with different IFO, n= 0~N-1

w[n]:White Gaussian noise, n = 0~N-1

The probability under white Gaussian noise is

$$p(x \mid H_i) = \frac{1}{(2\pi\sigma^2)^{\frac{N}{2}}} \exp(-\frac{1}{2\sigma^2} \sum_{n=0}^{N-1} x[n] - s_i[n])^2$$

The optimal H_i is chosen when

$$D_i^2 = \sum_{n=0}^{N-1} (x[n] - s_i[n])^2$$

Thus the optimal decision is

$$\hat{H}_i = \arg_i(\max(\sum_{n=0}^{N-1} x[n] s_i[n]))$$

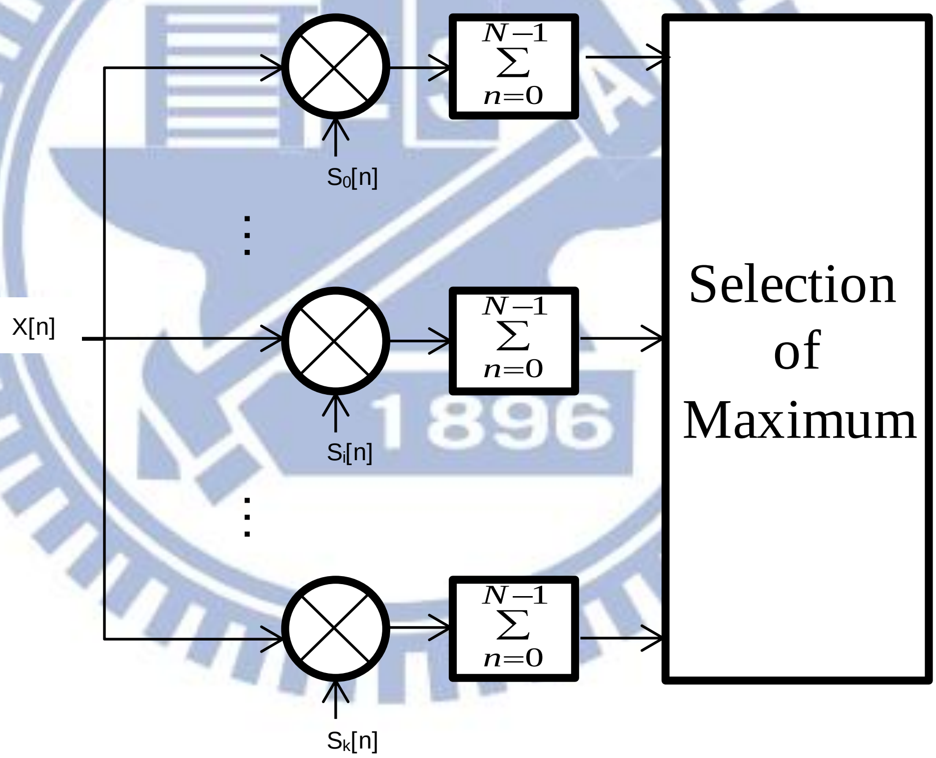

Fig. 3-10 Phase Ⅱ Estimator

Short preamble is the prior knowledge to the RX. To get $s_i[n]$ detector, we pre-distort the short preamble with specific frequency offset, as shown in Fig. 3-11. For example, to get 8000ppm detector, we pre-distort short preamble with 8000pppm frequency offset.

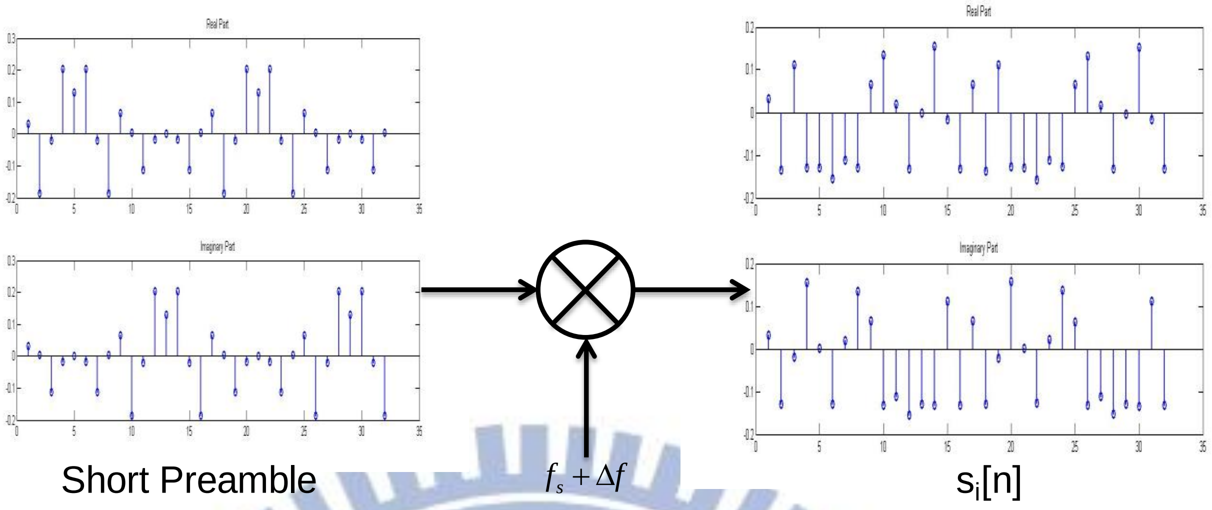

Fig. 3-11 Generation of detector coefficient

- De-Rotator

Estimator Ⅱ decides the frequency offset according to smallest distance between incoming distorted short preamble and specific detector $s_i[n]$. To make incoming short preamble closer to the $s_i[n]$, de-rotator compensates the short preamble due to the value from estimator Ⅰ. The overall procedure is shown in Fig. 3-12. Assume original short preamble has -9000ppm frequency offset. Ideally, estimator Ⅰ gets value -1187.5ppm, and de-rotator compensate this frequency offset, making the remaining frequency offset locate on -8000ppm detector. Finally the total frequency offset is combination of estimated value from estimator Ⅰ and estimator Ⅱ, which is -1187.5ppm + -8000ppm equals -9000ppm.

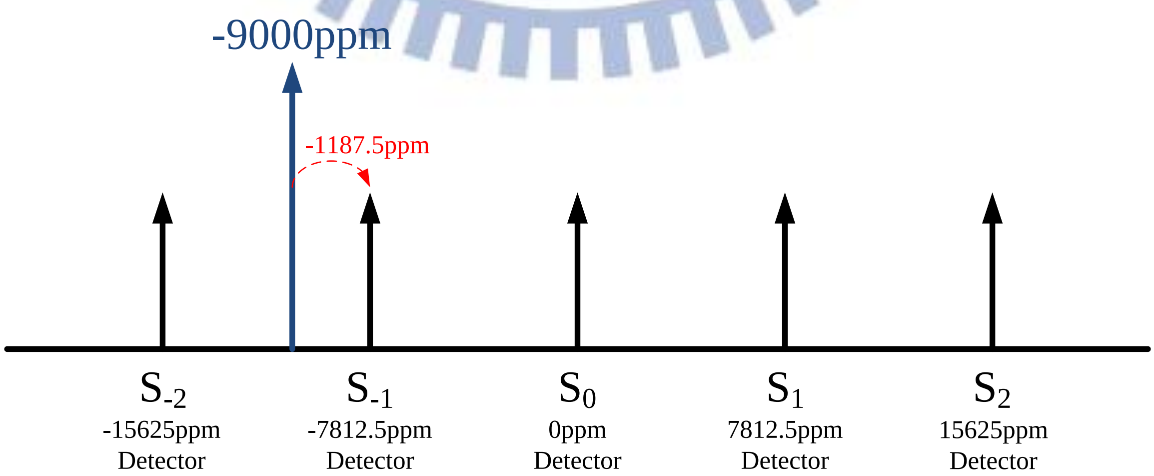

Fig. 3-12 Clock calibration example

- Boundary Detection

After the packet detection, we get the rough timing information of coming packet. However, we still need further timing information in order to derive ISI-free DFT-window for later channel estimation, SIG decoding, and data demapping.

Conventional boundary detection uses cross-correlation algorithm Equation(3-7). The receiver correlates the received signal with ideal pre-known waveform (such as GI2 in preamble). The boundary is found when cross-correlation value is larger than threshold, as shown in Fig. 3-13

$$\vartheta(m) = \left| \sum_{r=0}^{R-1} z_{m-r} x_{m-r-L}^{*} \right| \qquad (3\text{-}7)$$

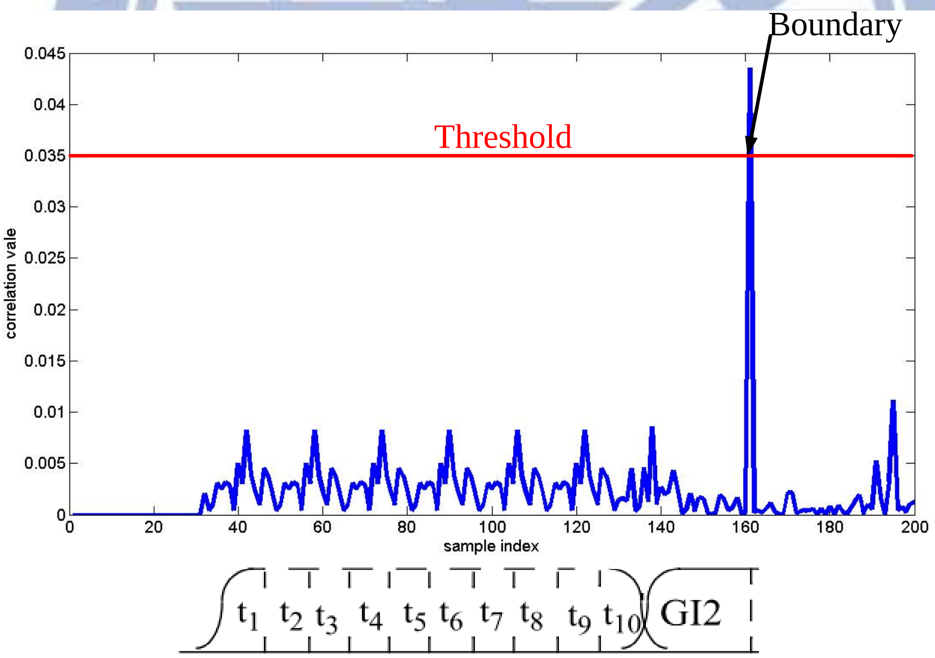

Fig. 3-13 Conventional cross-correlation

However, frequency offset of on-chip oscillator deteriorates the received signal, which decreases the correlation value significantly. Moreover, the multipath effect causes the uncertainty of the peak of correlation value as shown in Fig. 3-14.

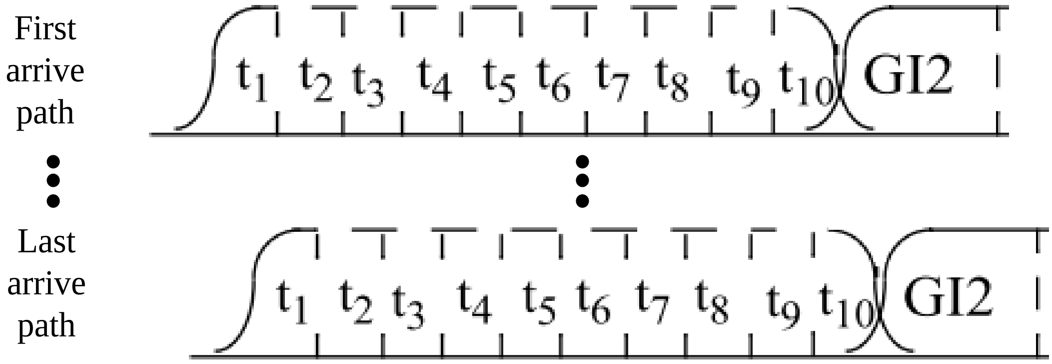

Fig. 3-14 Multipath effect

Due to the above problems, we use dual-correlation algorithm to do the boundary detection. It combines both auto-correlation and cross-correlation algorithm, and in auto-correlation part, it averages over some short preamble symbols to combat the magnitude attenuation due to clock frequency offset. The boundary detection algorithm is shown in Equation(3-8). z is the received signal. x is the ideal short preamble. N is short preamble size 16. R is the auto-correlation window which equals to 16.

$$\phi(m) = \sum_{l=0}^{L-1} \left| \sum_{r=0}^{R-1} z_{l\times N+m-r} z^{*}_{l\times N+m-r-L} \right|$$
$$\vartheta(m) = \left| \sum_{r=0}^{R-1} z_{m-r} x^{*}_{m-r-L} \right| \qquad (3\text{-}8)$$

Boundary is detected when

$$\phi(m) < Threshold\_1$$
$$\vartheta(m-L) > Threshold\_2$$

The waveform is shown in Fig. 3-15

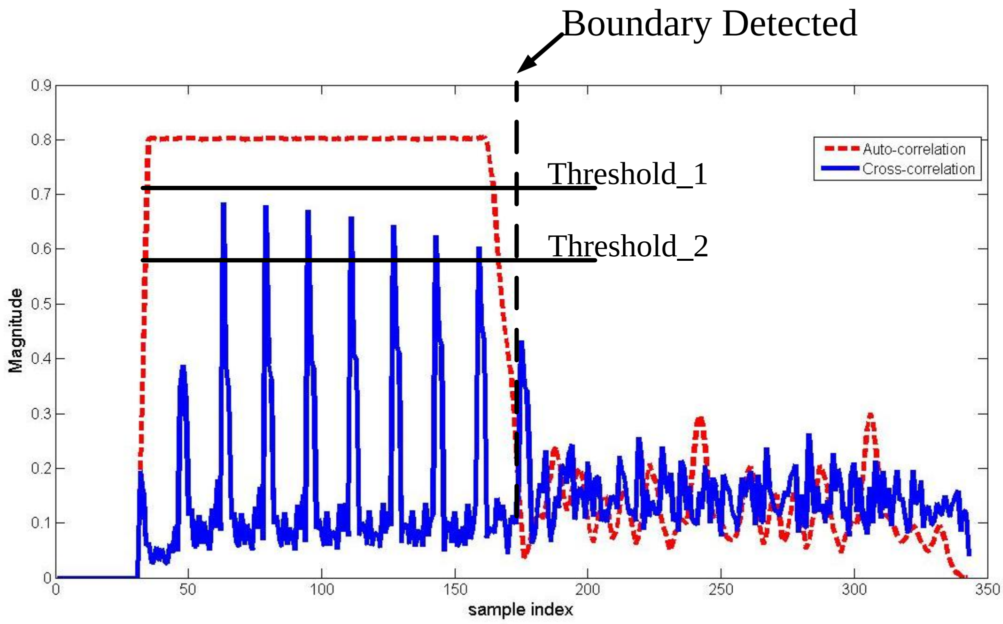

Fig. 3-15 Dual correlation waveform

3-3.3 Channel Equalization

The measurement result in Fig. 3-16 shows that body channel is selective, thus we need channel equalizer to make it flat. The algorithm we choose is zero forcing, as shown in equation(3-9). We use received long preamble, compared it with ideal long preamble. The comparison result is estimated channel. Then the incoming signal divided by estimated to make it response flat.

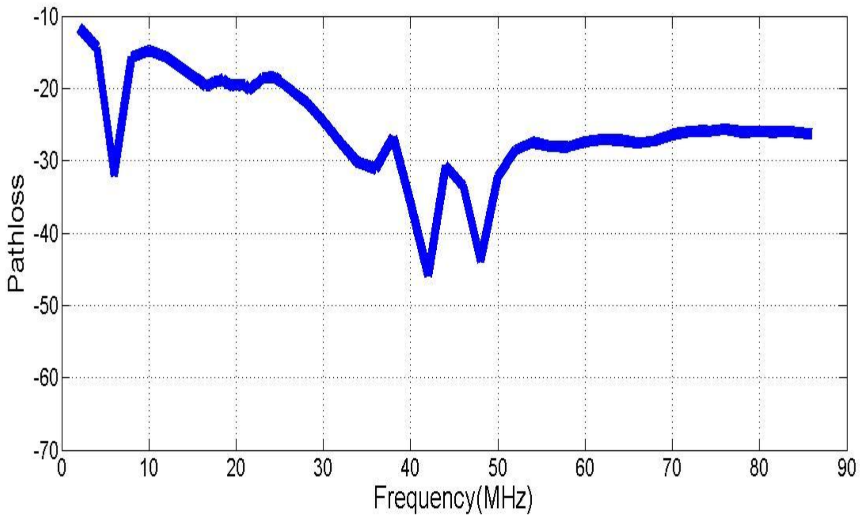

Fig. 3-16 Frequency response

$$C_k = LP'_k / LP_k$$
$$Z'_k = Z_k / C_k \qquad (3\text{-}9)$$

C_k = channel frequency response

LP_k = ideal long preamble

LP'_k = received long preamble

Z_k = incoming signal

Z'_k = signal after equalization

3-3.4 Post-FFT Compensation

In the time domain, we have done the clock calibration and fine carrier frequency offset calibration. However, due to noise, clock jitter, and some other defects, there still exists some residual offset in the system. Thus post-FFT compensation is needed. Equation(3-10) shows the frequency domain expression when there is residual offset exists. ε_F is carrier frequency offset (CFO), and δ_S is sampling clock offset(SCO). From equation(3-10) we can see that CFO and SCO causes phase shift for received signal, thus the distortion in phase is in equation (3-11), k is the sub-carrier index.

$$Z_{i,k} = X_{i,k} H_k \left[\frac{\sin(\pi\varepsilon_F)\sin(\pi\delta_S k)}{N^2 \sin(\frac{\pi\varepsilon_F}{N})\sin(\frac{\pi\delta_S k}{N})}\right] \times e^{j2\pi\left[\frac{i(N+N_g)+N_g}{N}(\varepsilon_F + k\delta_S)\right]} \qquad (3\text{-}10)$$

$$\theta_k = (\varepsilon_F + k\delta_S) \qquad (3\text{-}11)$$

Fig. 3-17 shows the frequency domain plot of phase. From the figure, we can see that CFO causes offset in phase and SCO results into slope in phase.

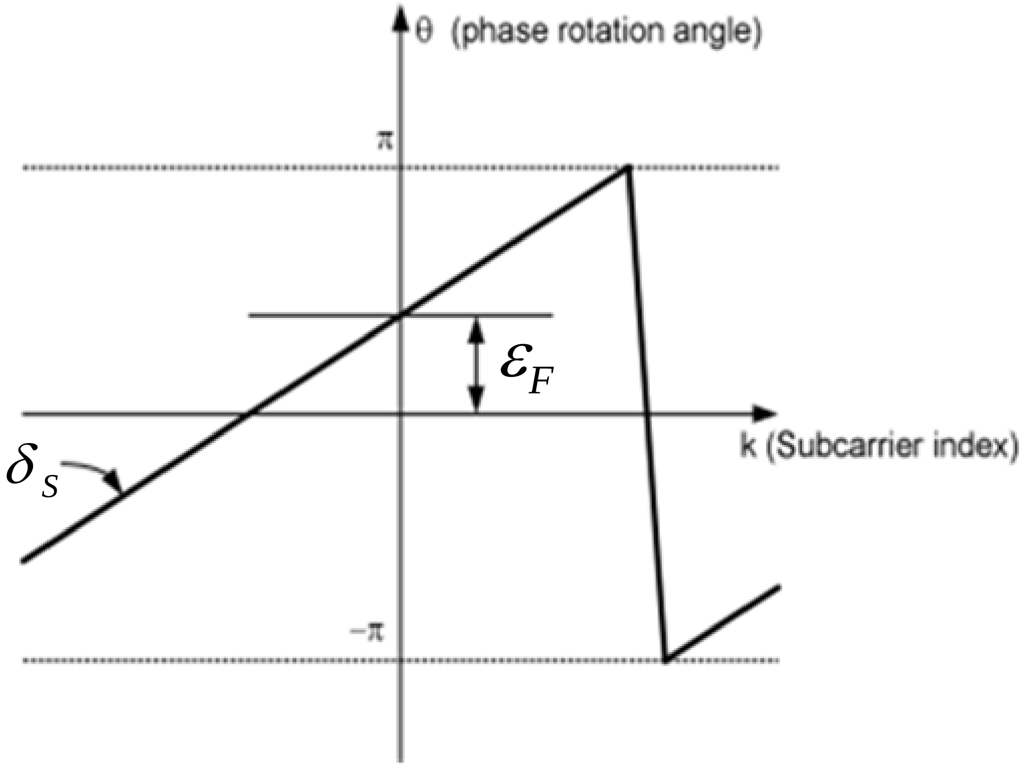

Fig. 3-17 Phase distortion in frequency domain

Here we use linear least square estimation to calculate the residual CFO and SCO. We can model distorted phase as equation

(3-12). The linear least square estimation solution is shown in equation(3-13)

$$\theta_k = H\begin{bmatrix}\varepsilon_F \\ \delta_S\end{bmatrix}, \quad H = \begin{bmatrix}1 & \ldots & 1 & \ldots & 1 \\ 0.. & & k\ldots & & (N-1)\end{bmatrix} \tag{3-12}$$

$$\begin{bmatrix}\varepsilon_F^{'} \\ \delta_S^{'}\end{bmatrix} = (H^T H)^{-1} H^T \theta_k \tag{3-13}$$

Because phase can only resolve into $\pm\pi$,

$$-\pi \prec 2\pi\Delta f\,(LN_s + N_g)(1+\eta)T + \frac{2\pi k}{N}(LN_s + N_g)\eta + \phi_k \prec \pi$$

where $\Delta f = f_c - f_c^{'}$, in our system T_S = 5MHz and f_c = 20MHz

Thus $\Delta f = 4(f_s - f_s^{'})$

$$\eta = \frac{T^{'} - T}{T} = \frac{1/f_s^{'} - 1/f_s}{1/f_s} = \frac{1/f_s^{'} - 1}{1} = \frac{f_s - f_s^{'}}{f_s^{'}}$$

$$-\pi \prec 2\pi(4\eta f_s^{'})(LN_s + N_g)(1+\eta)/f_s + \frac{2\pi k}{N}(LN_s + N_g)\eta + \phi_k \prec \pi$$

Since we compensate symbol by symbol, thus L = 1

In our system, sub-carrier size N = 64, cyclic prefix Ng = 4, k = 31, $\phi_k = 0$

Assume $f_s \approx f_s^{'}$

Thus

$$-\pi \prec 2\pi(4\eta)(LN_s + N_g)(1+\eta)_s + \frac{2\pi k}{N}(LN_s + N_g)\eta + \phi_k \prec \pi$$

Take all the numbers in

Finally, we get the estimation range is ± 1543 ppm, which is $\pm$ 7715Hz in 5MHz clock.

3-4 Simulation Result

Fig. 3-18 is the matlab simulation model. Here we use the body channel model from IEEE P802.15-08-0577-01-0006. Then AWGN is added to the signal and multiply CFO rotation. Finally using Resample to simulate SCO effect.

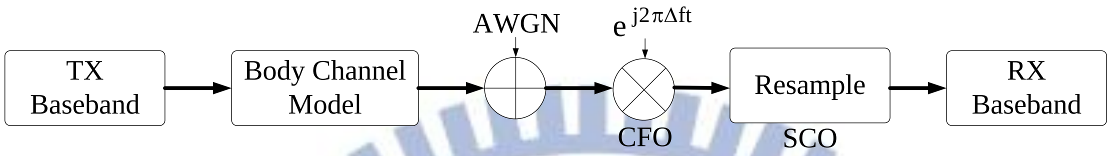

Fig. 3-18 Matlab simulation model

Fig. 3-19 shows the matlab simulation result with different initial clock offsets. Line with round marker corresponds to 0ppm clock offset, line with triangle marker corresponds to 10000ppm clock offset, and line with square marker corresponds to 20000ppm clock offset. Simulation result shows that there are a little BER degrade when clock offset gets larger and larger.

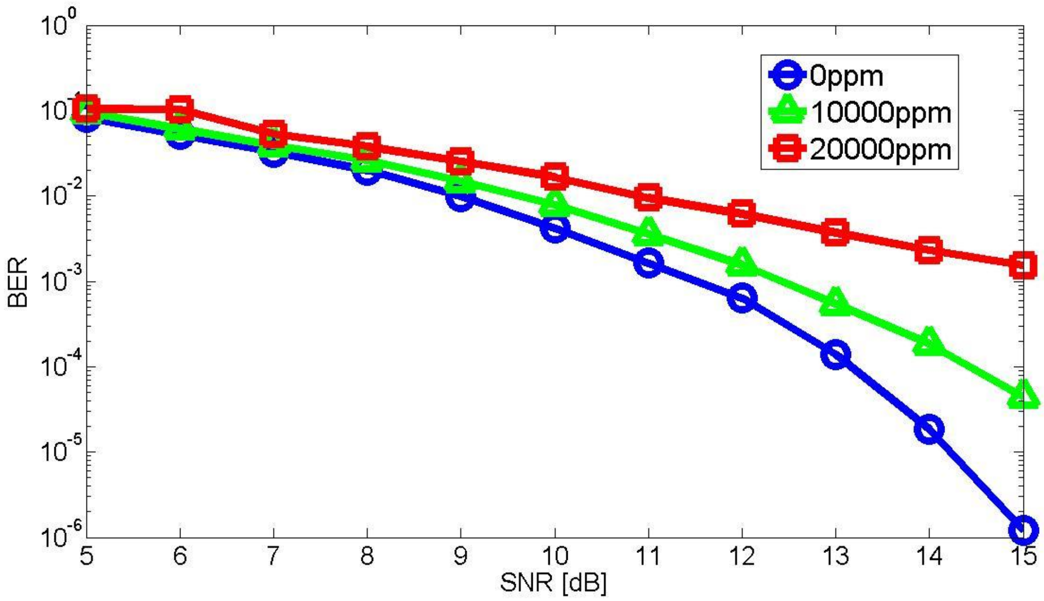

Fig. 3-19 Matlab simulation result with different clock offsets

Chapter 4: Implementation of Transceiver

Fig. 4-1 is the overall architecture for OFDM-based BCC transceiver, and Fig. 4-2 is the corresponding picture. It contains TX front-end, RX-front-end, and TRX baseband. TX baseband pattern feeds into DACs. DACs converts digital pattern to analog signal. According to human body frequency response, around 20MHz, channel response is flat and path-loss is small, which is suitable band for transmission. Thus modulator up-converts baseband signal to 20MHz. Then the driver matches the impedance of system to impedance of electrode. The TX signal is connected to body through electrode attached on skin. RX also uses electrode to collect transmitted signal from body. The DVGA tunes the input signal to certain voltage level, which is suitable for demodulation and later DSP processing. The collected signal is down-converted by demodulator to baseband. The baseband signal then goes through ADCs and is converted to digital signal and feed to RX baseband.

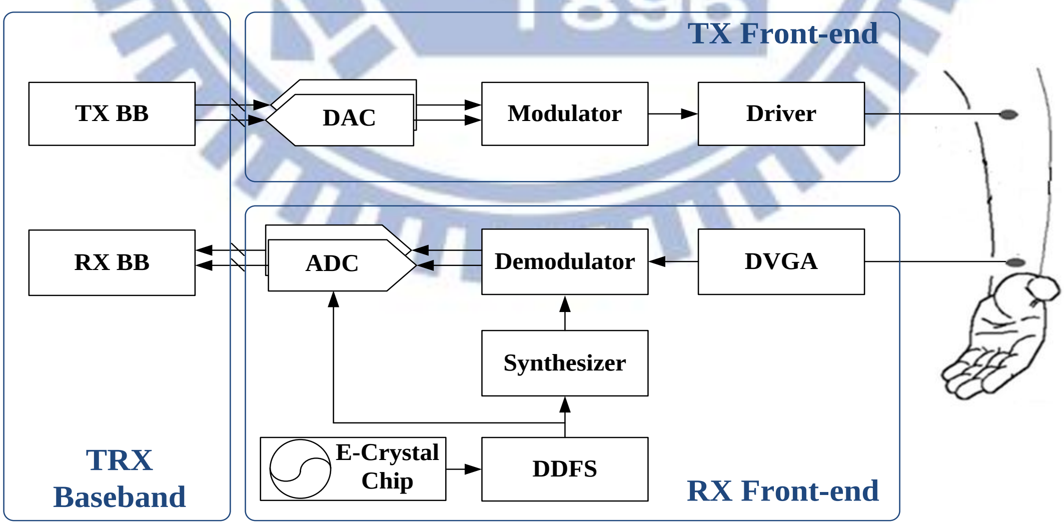

Fig. 4-1 Transceiver block diagram

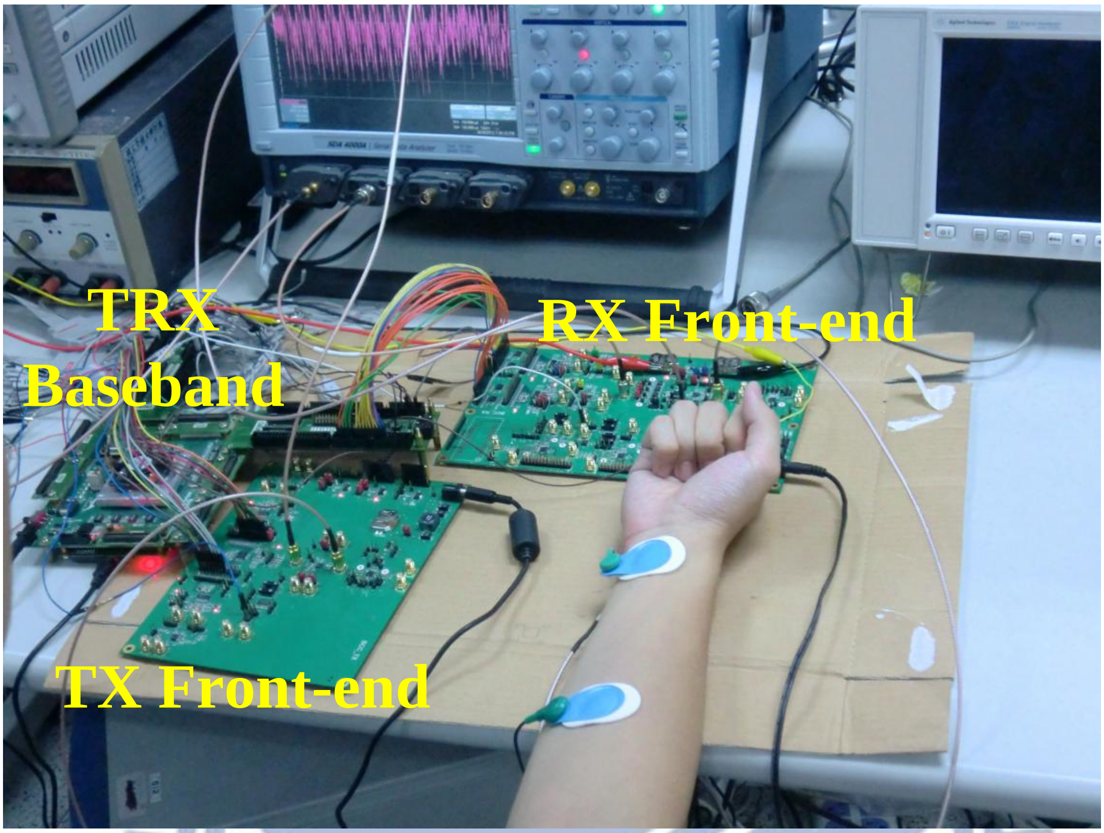

Fig. 4-2　　Emulation platform picture

4-1 Transmitter Front-end

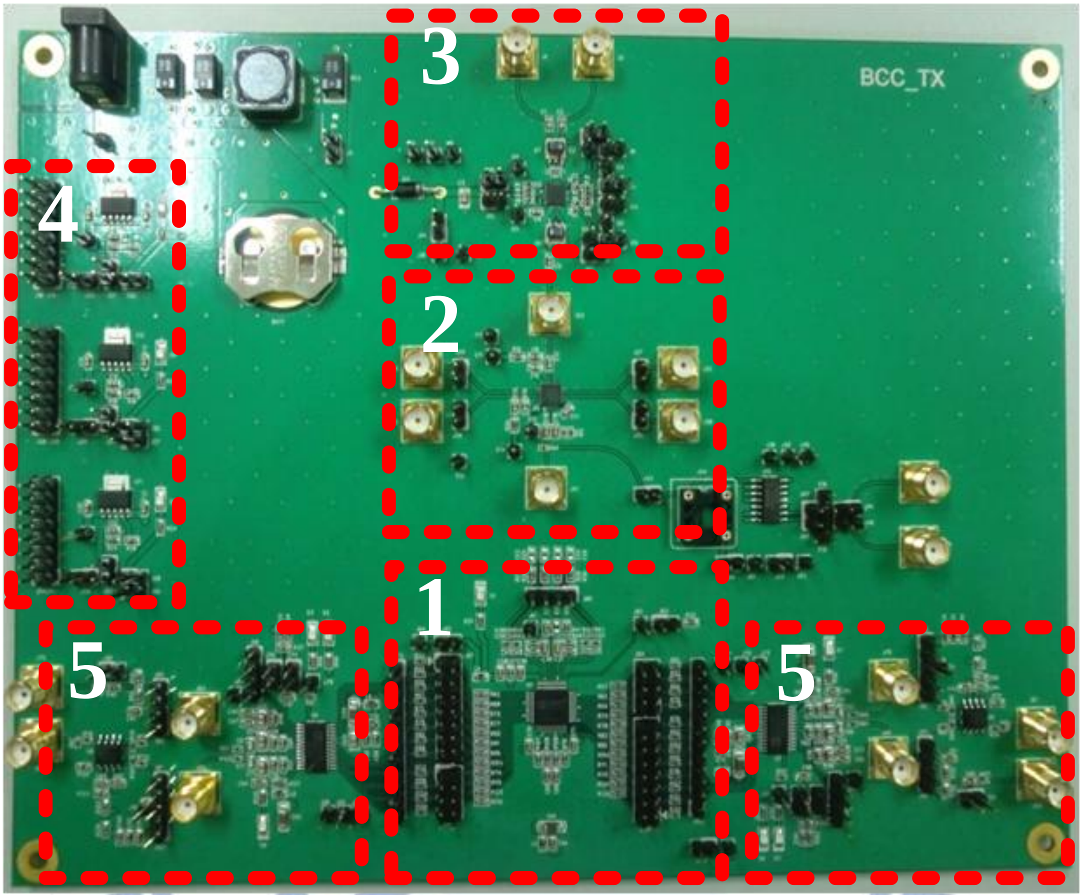

Fig. 4-3 Transmitter front-end picture, number 1 is DAC, number 2 is Mod, number 3 is Driver, number 4 is Power IC.

Table 4-1 Transmitter front-end components

Block Number	Function	Component	Specifications
1	DAC	AD9765	12bits / 5MHz
2	Modulator	LTC5598	RF 20MHz
3	Driver	LMH6515	200 Ohm
4	Power IC	RT9047	3.3V
5	ADC	AD9235	12bits / 5MHz

Fig. 4-3 is the picture of transmitter front-end, and Table 4-1 is the corresponding components table. Here we choose dual channel DAC. Its inputs are I and Q digital codeword, and outputs are I and Q differential analog waveform. Because the modulator baseband inputs are PNP BJTs with 0.5V DC bias, we add an offset in digital codeword to make DAC outputs have 0.5V DC bias. The modulator up-converts baseband signal to 20MHz RF signal and then feed RF signal to driver. From [7](Fig. 4-4), we can see that contact impedance of human body with different metal electrodes. at 20MHz, is around 200 Ohm, thus the drive with 200 Ohm output impedance is chosen to match the contact impedance.

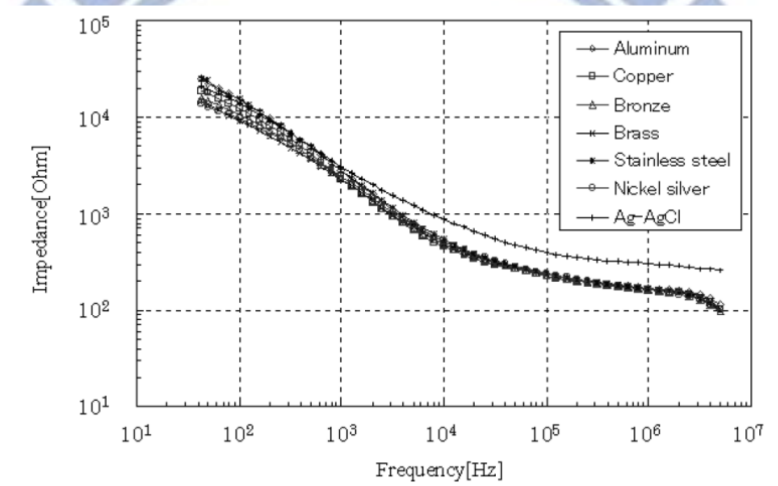

Fig. 4-4 Impedance frequency response

Since the device is designed to be portable, thus in power planning, besides from normal DC plug input, it can also uses battery as power input. The schematic of power planning is shown in Fig. 4-5

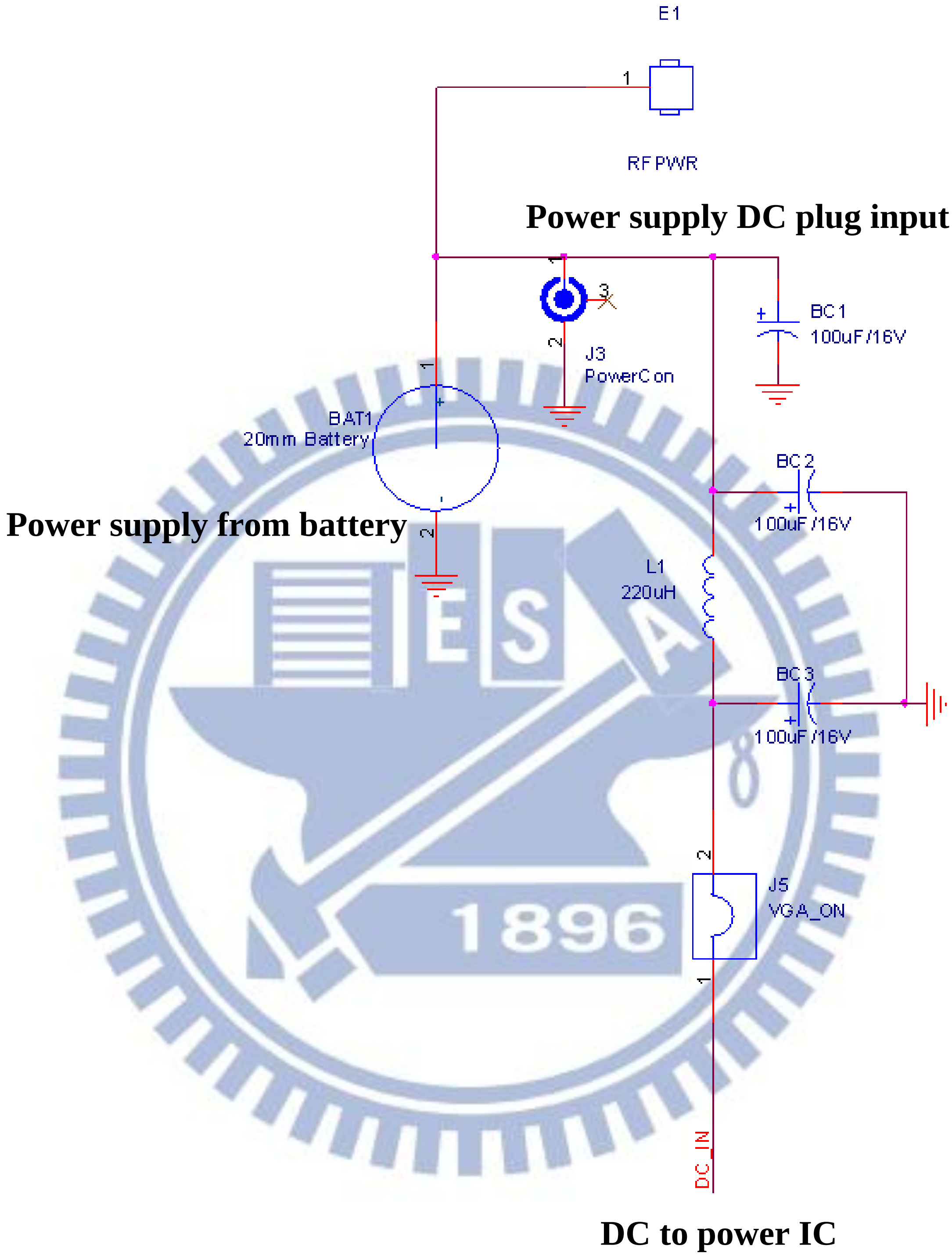

Fig. 4-5　　Power planning

4-2 Receiver Front-end

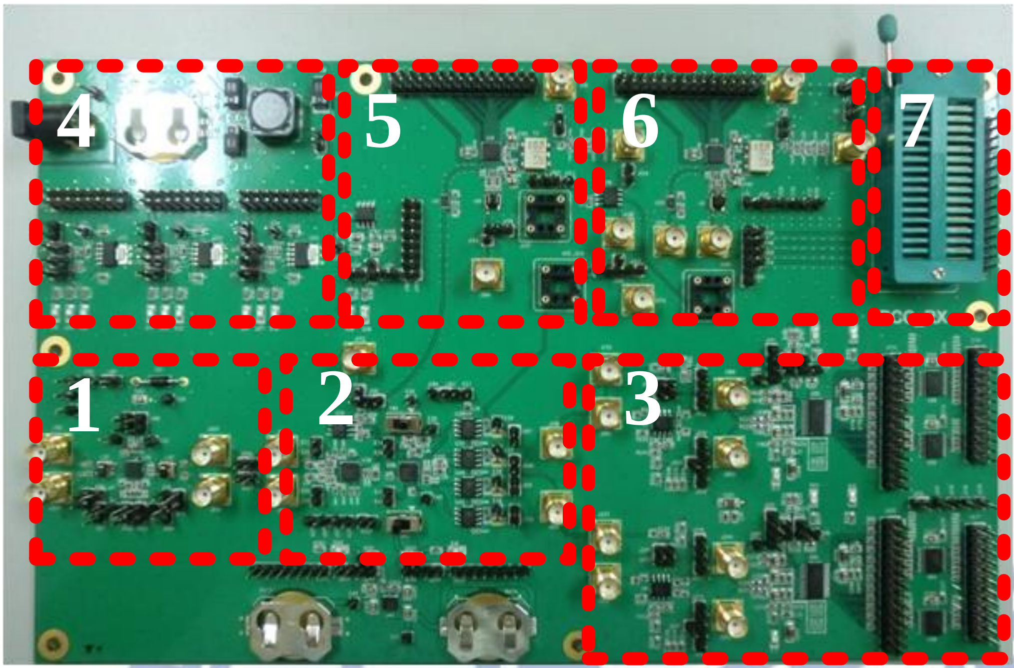

Fig. 4-6 Receiver front-end picture, number 1 is DVGA, number 2 is Demod, number 3 is ADC, number 4 is Power IC, number 5 is Synthesizer, number 6 is DDFS, number 7 is e-Crystal socket

Table 4-2 Receiver front-end components

Block Number	Function	Component	Specifications
1	DVGA	AD9765	200 Ohm
2	Demodulator	AD8333	RF 20MHz
3	ADC	AD9235	12bits / 5MHz
4	Power IC	RT9047 RT9183 LT3032	3.3V / 5V / 1V
5	Synthesizer	AD9913	80MHz
6	DDFS	AD9913	Tuneable frequency
7	e-Crystal socket	32-DIP socket	

Fig. 4-6 is the picture of transmitter front-end, and Table 4-2 is the corresponding components table. From chapter 2.1-3, we know that path-loss varies with transmission scheme and transmission distance. Thus a DVGA is included in the system. The gain of DVGA is controlled by baseband digital codeword, which is calculated by VGA block. Also, the input impedance of DVGA is 200 Ohm to match the contact impedance of human body with electrode. The demodulator down-converts the 20MHz RF signal to baseband signal. Specially note that local oscillator (LO) of demodulator should be 4 times the RF frequency. For example, 20MHz RF signal should have LO frequency equals to 80MHz. Following is ADC to transfer analog waveform into digital codeword for baseband processing. To emulate with e-Crystal chip, 32-DIP socket is included. The e-Crystal clock feeds to DDFS, which is frequency tunable with digital codeword from baseband clock calibration block.

There are two important issues in layout of PCB, symmetry and shielding. OFDM system has I and Q channel, symmetric layout for those two channels is very important.

- IQ imbalance

Following is the analysis of IQ imbalance in OFDM system.

Fig. 4-7 is the basic block diagram for direct-conversion receiver.

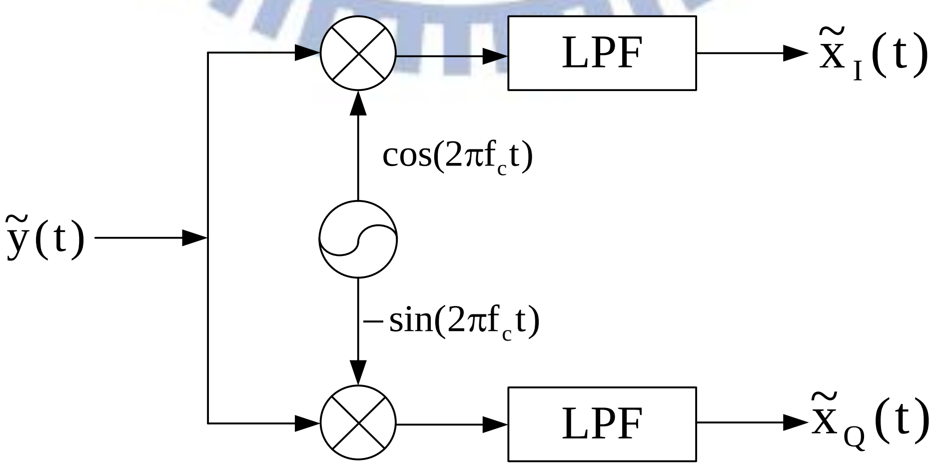

Fig. 4-7 Direct conversion receiver

Ideally the passband signal can be expressed as Equation (4-1)

$$\breve{y}(t) = \mathrm{Re}\{x(t)e^{j2\pi f_c t}\} = x_I(t)\cos(2\pi f_c t) - x_Q(t)\sin(2\pi f_c t) \qquad (4\text{-}1)$$

Assume system exists gain error $\frac{1+\alpha}{1-\alpha}$ and phase error ϕ, we model those imbalance into LO, and the express the LO output as equation(4-2)

$$\begin{aligned} &2(1+\alpha)\cos(2\pi f_c t - \phi/2) \\ &-2(1-\alpha)\sin(2\pi f_c t + \phi/2) \end{aligned} \qquad (4\text{-}2)$$

Thus the baseband signal due to imbalance is

$$\begin{aligned} \tilde{x}_I(t) &= (1+\alpha)[x_I(t)\cos(\frac{\phi}{2}) - x_Q\sin(\frac{\phi}{2})] \\ \tilde{x}_Q(t) &= (1-\alpha)[x_Q(t)\cos(\frac{\phi}{2}) - x_I\sin(\frac{\phi}{2})] \\ \tilde{x}(t) &= \tilde{x}_I(t) + j\tilde{x}_Q(t) \\ &= [\cos(\frac{\phi}{2}) + j\alpha\sin(\frac{\phi}{2})]x(t) + [\alpha\cos(\frac{\phi}{2}) - j\sin(\frac{\phi}{2})]x^*(t) \\ &= Ax(t) + Bx^*(t) \end{aligned} \qquad (4\text{-}3)$$

To analyze the effect in frequency domain, we know that $(X_k)^* = X_{-k}^*$

Thus

$$\tilde{X}_k = AX_k + BX_{-k}^* \qquad (4\text{-}4)$$

From Equation(4-4), we can see that IQ balance in frequency domain not only has complex gain on the carrier, but also introduces ICI to the carrier.

Fig. 4-8 shows a time domain short preamble waveform, blue waveform is from I channel and green waveform is from Q channel, which has IQ gain mismatch around 1dB.

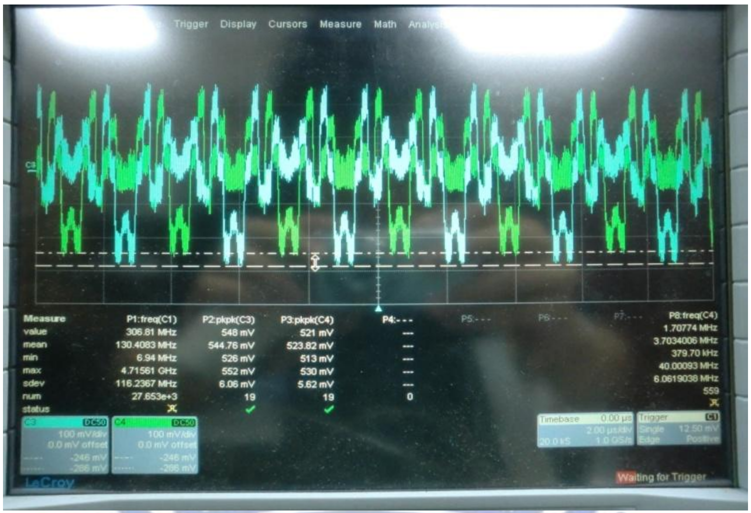

Fig. 4-8　　IQ gain mismatch

To combat this problem, we reserve path for attenuator on I and Q, and manually tune the gain by inserting attenuator in I and Q path, as shown in Fig. 4-9. For example, if measurement result shows that I channel is 1dB larger than Q channel, then we insert 1dB attenuator in I channel and 0dB attenuator in Q channel to make two path balance.

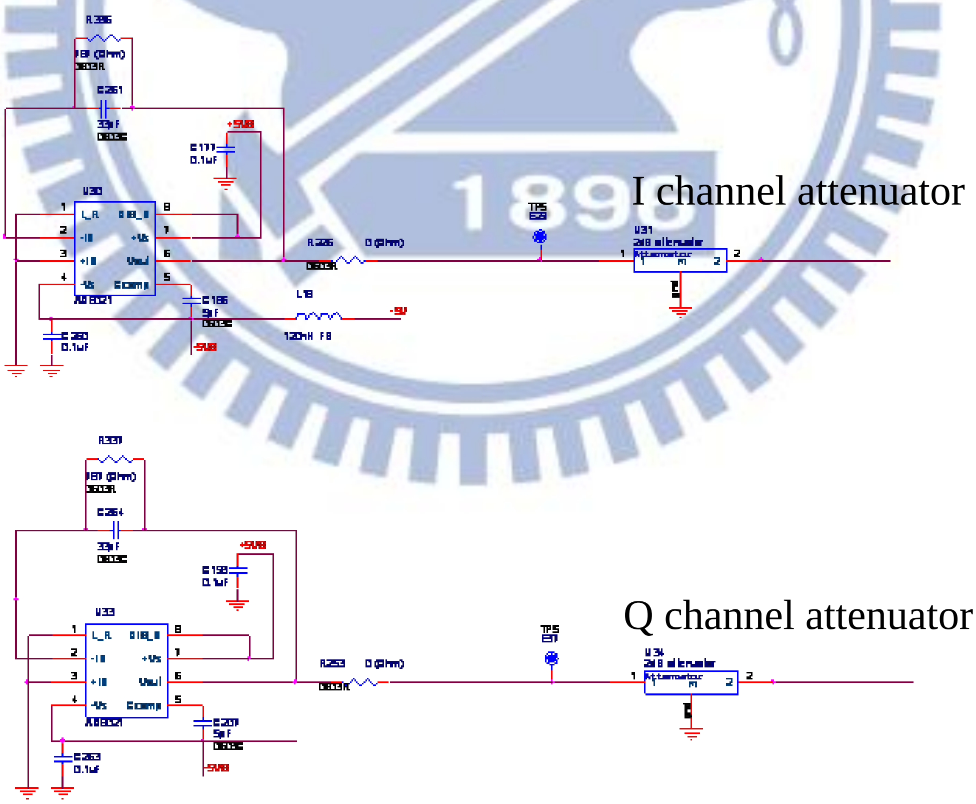

Fig. 4-9　　I and Q channel attenuator

➢ RF shielding

In our system, there are many components with different operation frequency. To avoid interference from each other, carefully RF shielding is needed. Fig. 4-10 shows demodulator output short preamble waveform with RF coupling interference from LO.

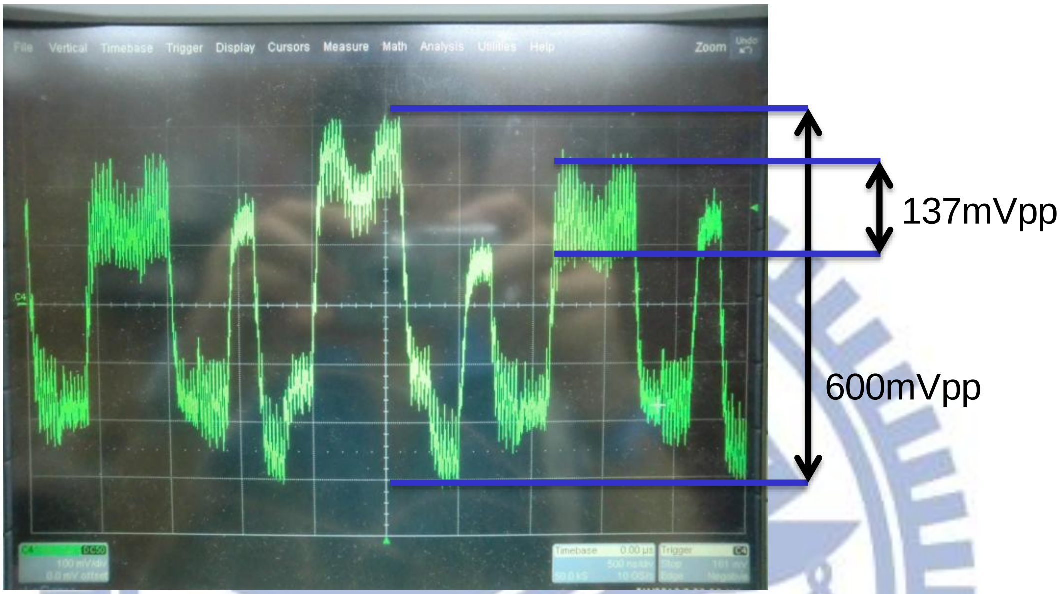

Fig. 4-10 Coupling interference

To combat this problem, we add many via along the RF path and PCB board to avoid the coupling interference, as shown in Fig. 4-11.

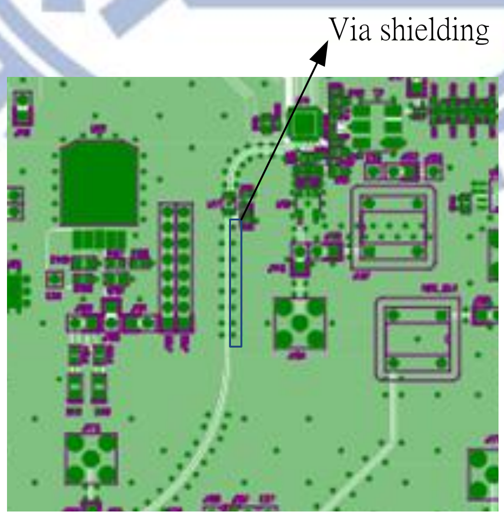

Fig. 4-11 Via shielding

4-3 Emulation of Clock Drift Calibration

The emulation flow of clock drift calibration is shown in Fig. 4-12. Assume originally there is clock drift in e-Crystal chip, which is 0.020MHz drift from ideal 5MHz clock frequency. This drifted clock feed into DDFS. The output of DDFS servers as ADC reference input and synthesizer input. The synthesizer multiplies input frequency by 5 times, which makes LO frequency of Demodulator equals 80.32MHz. When preamble comes into system, clock calibration block in RX BB calculates the frequency offset, and then sends corresponding DDFS tuning codeword to tune the DDFS. After DDFS receive digital tuning codeword, its frequency is tuned to be 5MHz, thus compensates the clock drift from e-Crystal chip.

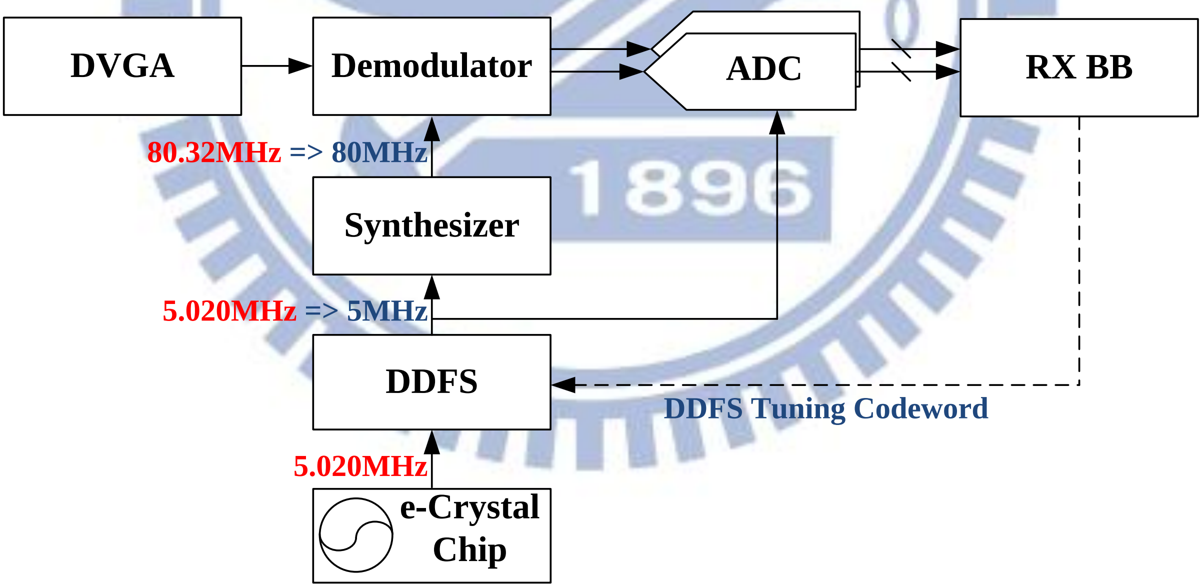

Fig. 4-12 Clock calibration emulation flow

The emulation result is shown in Fig. 4-13. Fig. 4-13 (a) is the initial DDFS output before calibration, Fig. 4-13 (b) is the initial DDFS output after calibration. Fig. 4-14 (a) is the short preamble output before calibration, Fig. 4-14(b) is the short preamble output after calibration.

We can see form those figures that before calibration, there is clock frequency offset and the short preamble pattern is distorted. After calibration, the clock frequency is corrected and the short preamble is restored.

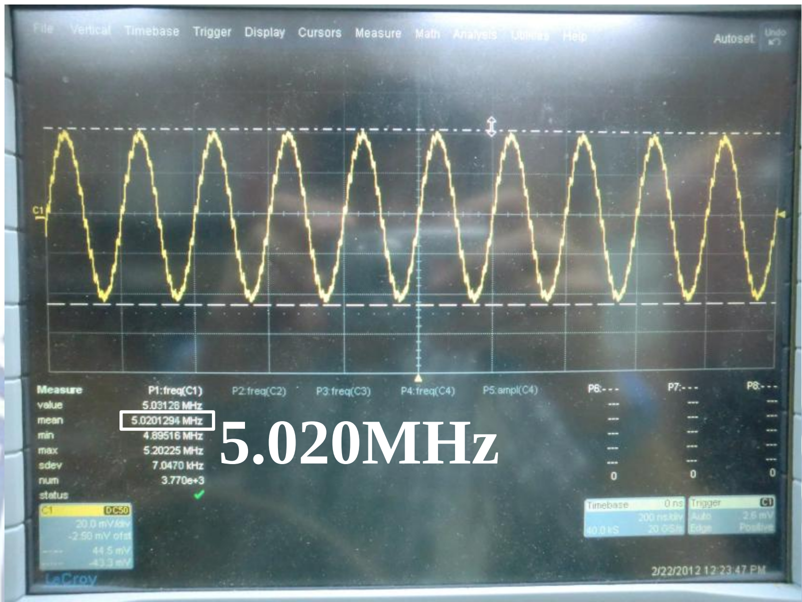

(a)

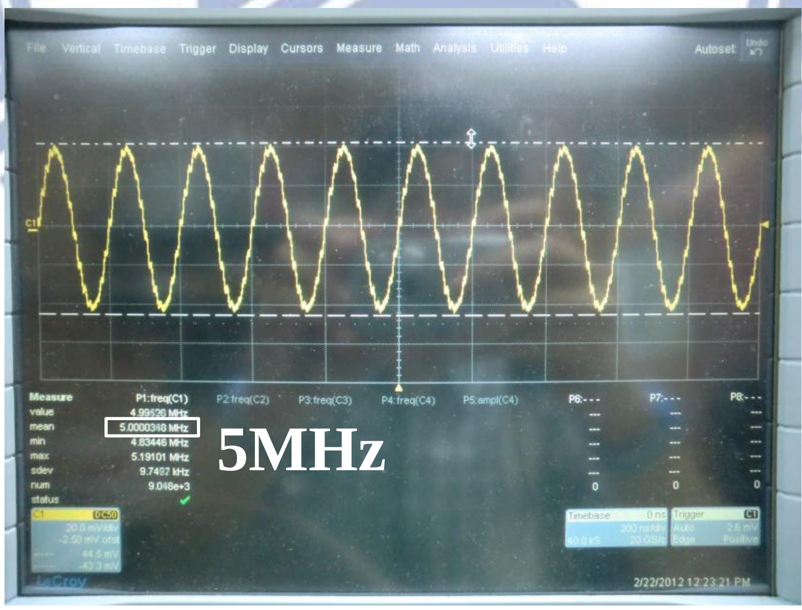

(b)

Fig. 4-13 DDFS ouput (a)Before calibration, (b)After calibration

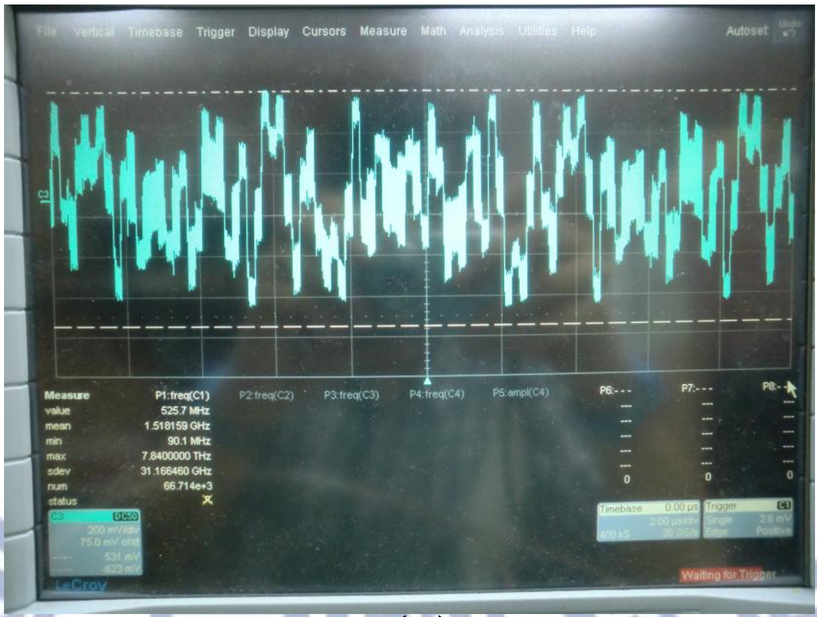

(a)

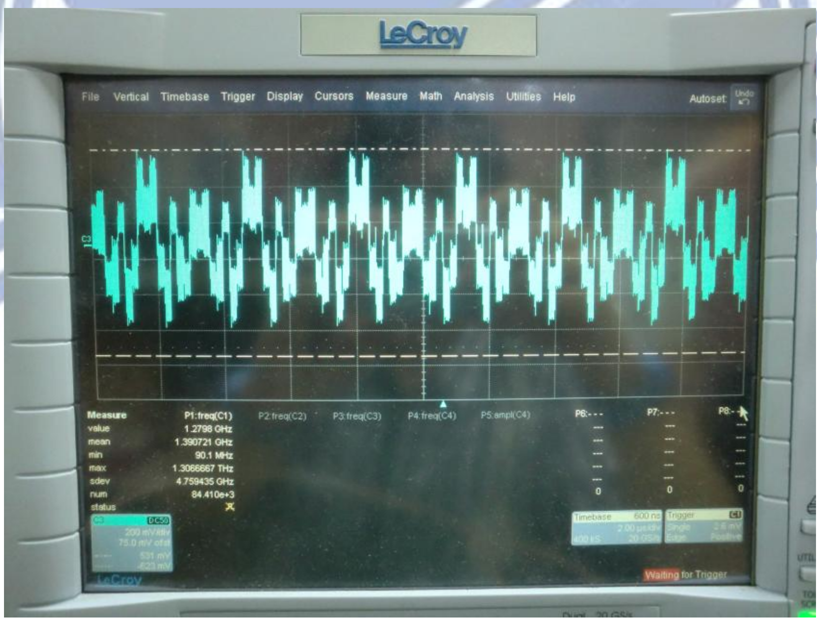

(b)

Fig. 4-14 Short preamble waveform(a) Before calibration, (b)After calibration

4-4 Emulation of AGC

Fig. 4-15 is the emulation flow of AGC. Assume initially the input voltage swing is smaller than expected. The VGA block in RX BB calculates the gain using the input preamble, and according to the gain, sends the corresponding DVGA tuning codeword to tune the gain of DVGA.

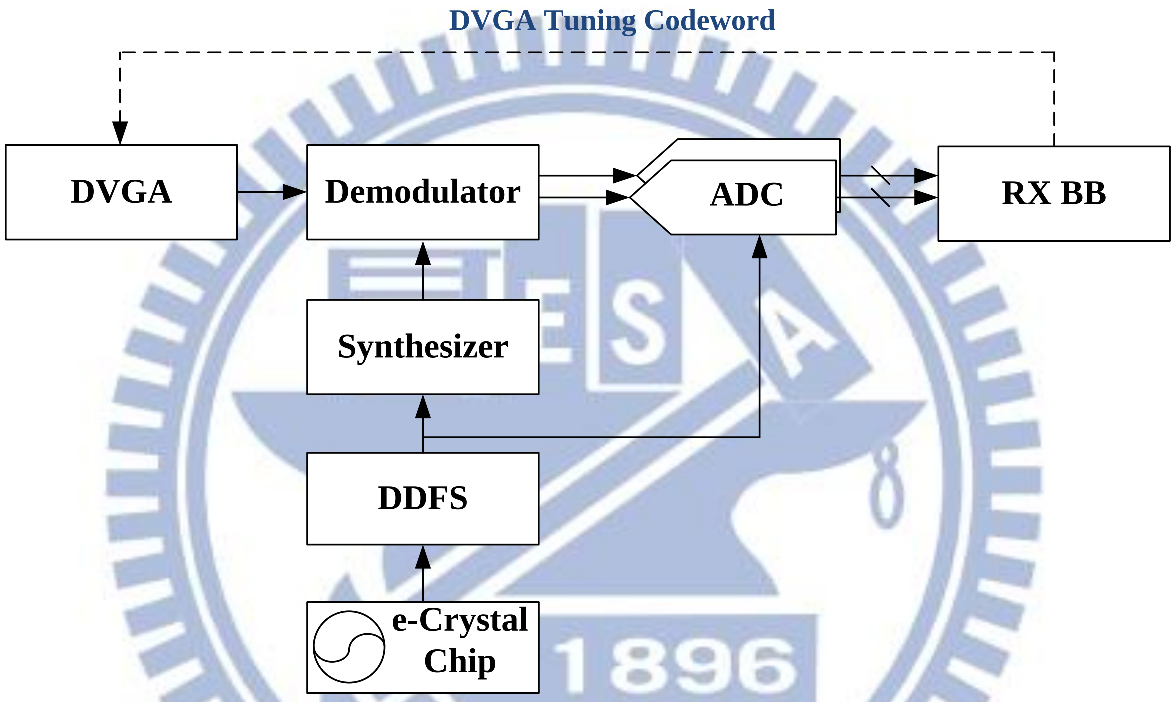

Fig. 4-15 AGC emulation flow

Fig. 4-16 shows the emulation result. Originally, input short preamble voltage swing is smaller than expected. After tuning DVGA, the swing goes to expected value.

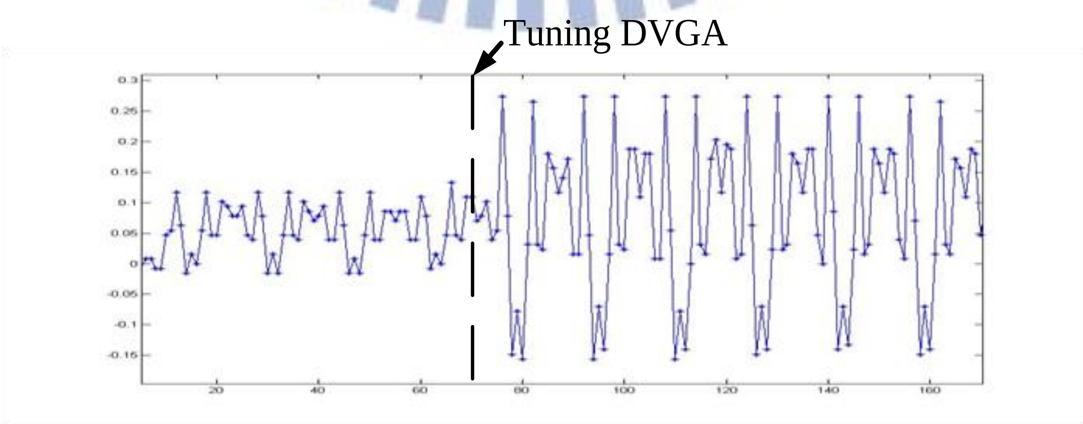

Fig. 4-16 Emulation result

Chapter 5:
Experiment Result

5-1 Measurement Result

This chapter shows the experiment result. Fig. 5-1 is the TX DAC output. The format of the waveform is also shown below. Then Fig. 5-2 is the TX MOD output. We can clearly see that the waveform contains high frequency part, which is waveform in Fig. 5-1 modulating with 20MHz sin wave. Fig. 5-3 is the RX ADC output. It has a little distortion, which comes from noise and interference. Fig. 5-4 is the received baseband signal. The baseband word length is 8 bits and word depth is 9 bits. The detection of arriving of the packet is done when receiver baseband receives 10 repetitive short preambles. Then the AGC, and clock calibration process after packet detection. GI2 is used for boundary detection. Following is 2 identical long preambles which are used for channel estimation and fine-CFO estimation. Two SIG packets show the size of payload. Finally is the payload which contains the data.

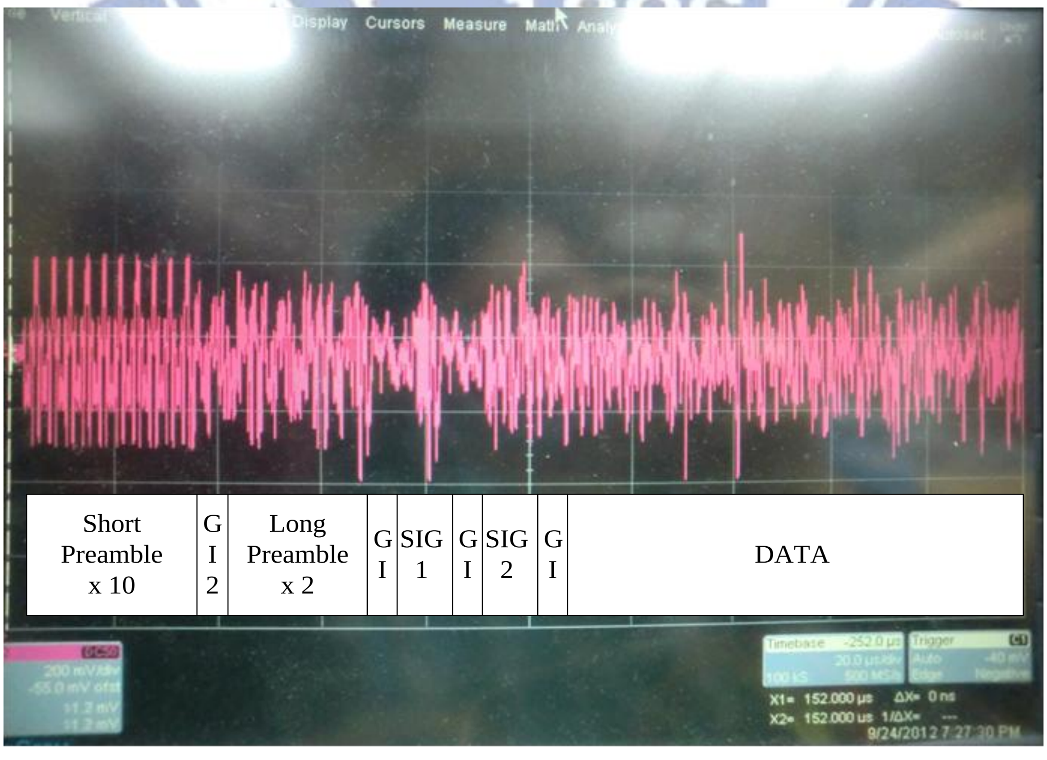

Fig. 5-1 DAC output

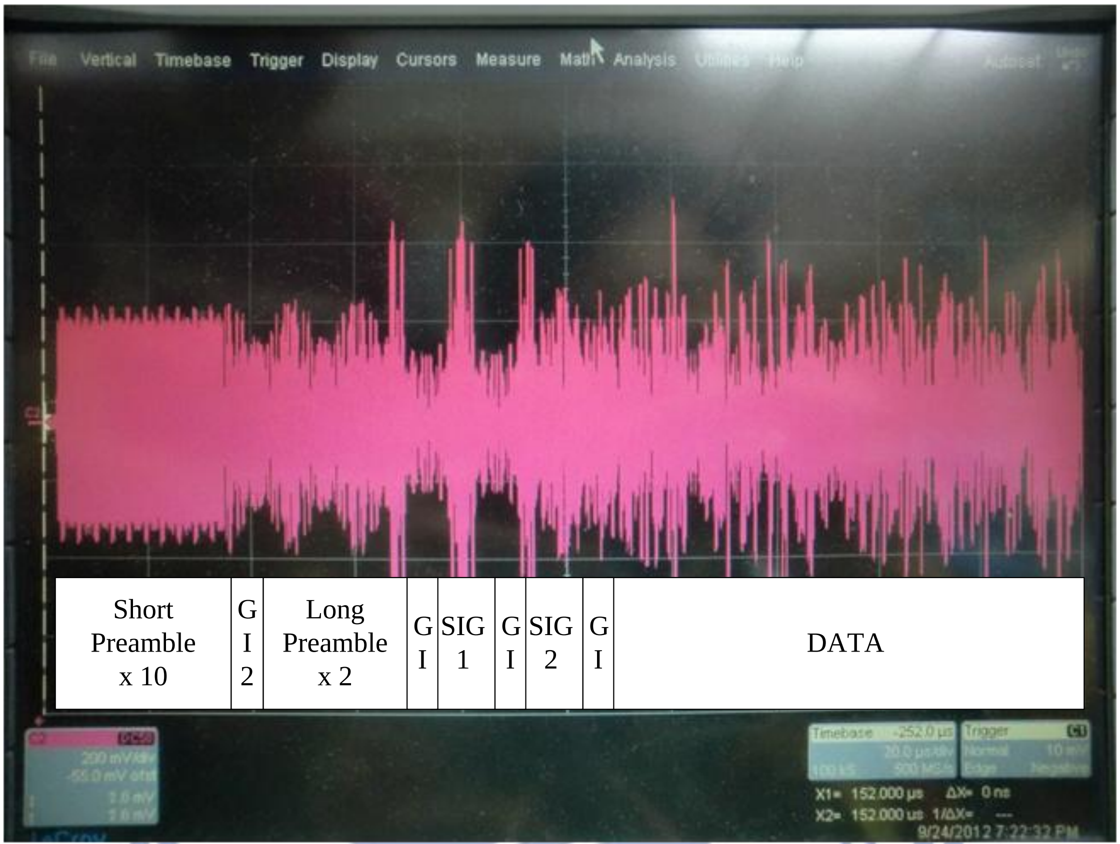

Fig. 5-2 MOD output

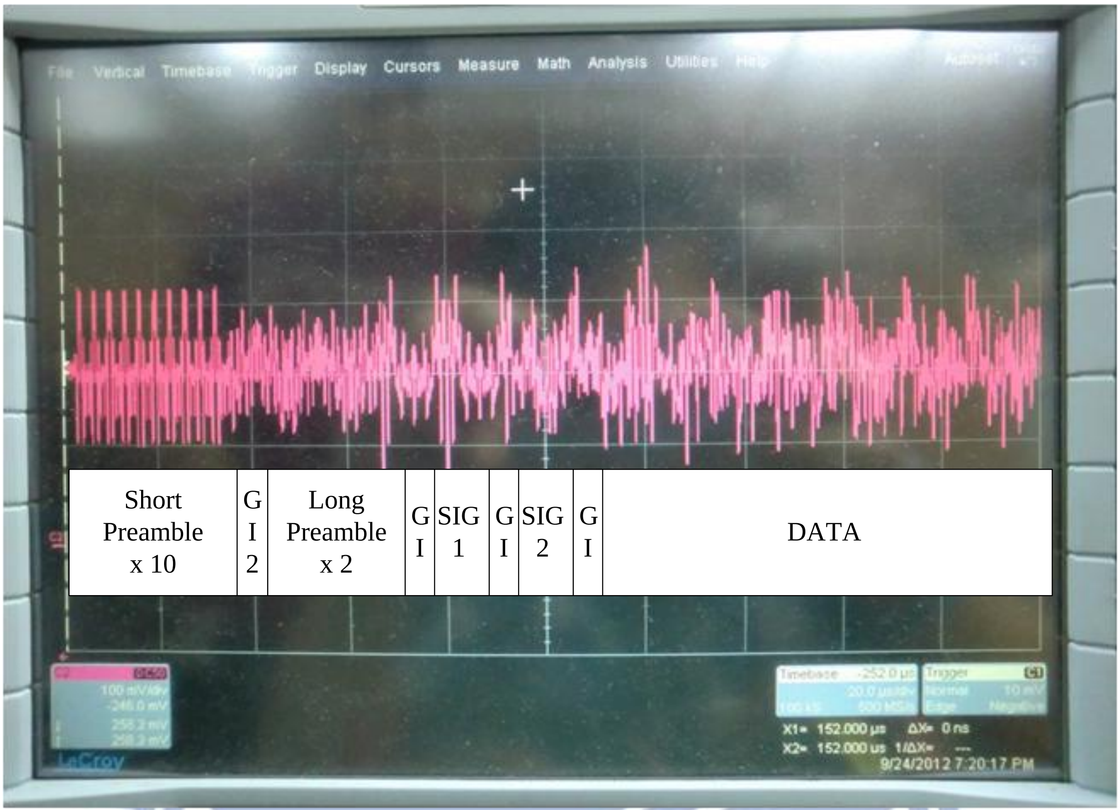

Fig. 5-3 ADC output

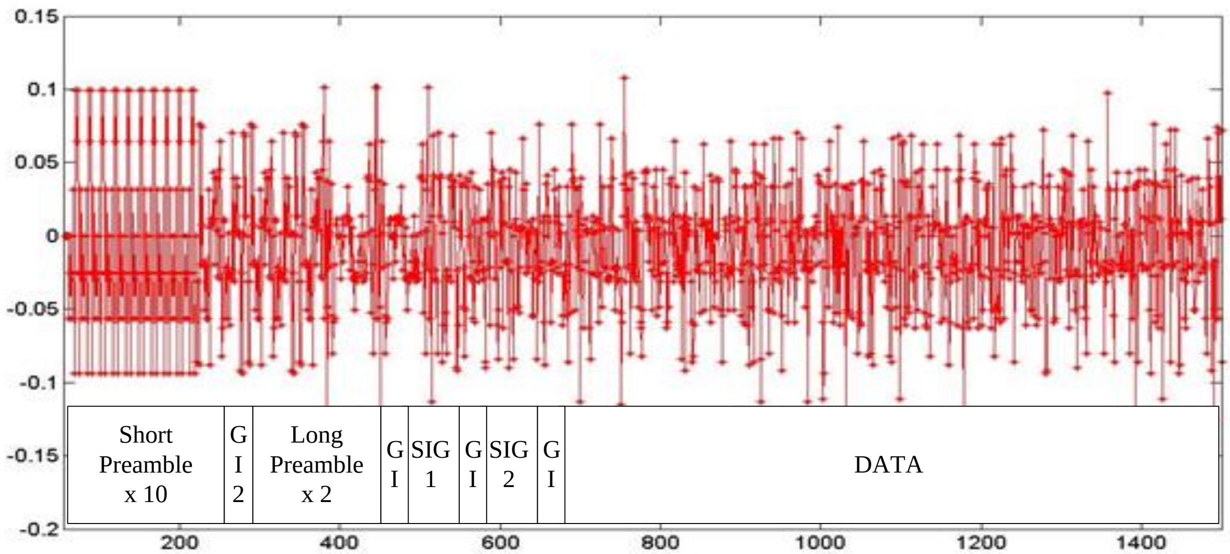

Fig. 5-4 Received baseband signal

Fig. 5-5 is the experiment result under different conditions. In condition 1 and condition 2, two sensors are attached on one arm with distance 10cm and 30cm, and the BER performance of these two conditions is close to each other. However, when two sensors are across arm, as shown in condition 3, the BER degrades a lot. This is probably due to when two sensors are far from each other, the interference comes from body antenna effect is more severe.

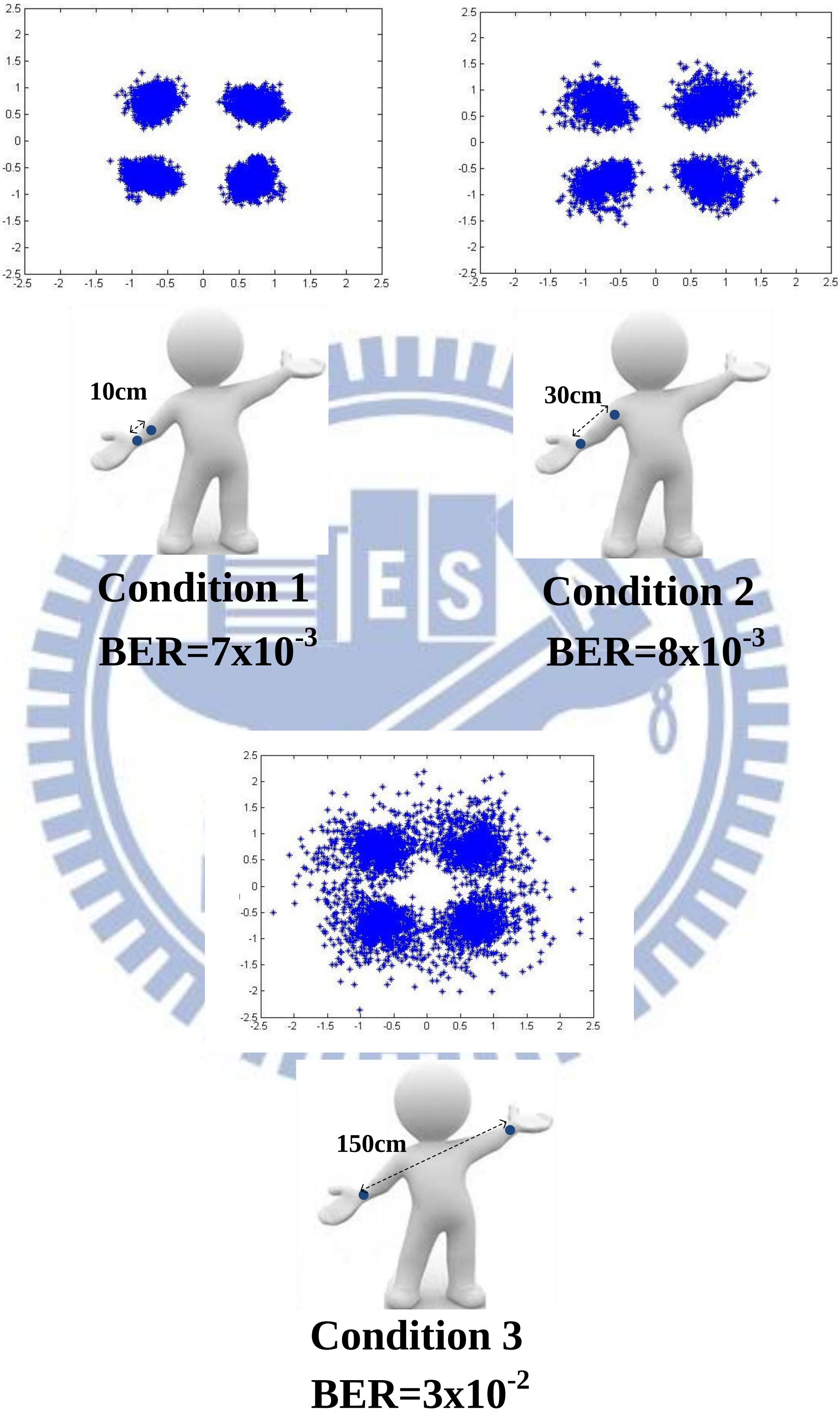

Fig. 5-5 Constellation and BER under different condition

5-2 Comparison Result

Table 5-1 is the comparison of BCC systems. It compares modulation scheme, frequency band, data rate, and oscillator type. From the comparison, we can see this work achieve high data rate with better spectral efficiency, and on chip oscillator integration to provide smaller area and more comfortable wearing. The all digital e-Crystal on-chip oscillator is portable with process migration.

Table 5-1 Compared with other BCC systems

Publication	This work	ISSCC'07[1]	JSSC'09[3]	ASSCC'10[13]
Modulation	OFDM	PAM	FSK	FSK
Freq. Band (MHz)	17.5 ~ 22.5	1 ~ 200	30 ~ 70	20 ~ 40
Data Rate (Mbps)	6.7	2	5	1
Spectral Efficiency (bps/Hz)	1.34	0.01	0.125	0.05
Oscillator	e-Crystal (All digital)	All digital	LC DCO	LC DCO
Process Migration	Portable	Portable	Non-Portable	Non-Portable

Chapter 6:
Conclusion and Future Work

6-1 Conclusion

This thesis presents a body channel communication emulation platform. With the dedicated OFDM transmission strategy, which transmits collected data in one shot and then turns the system into sleep mode on the other time, high data rate with low operation energy can be achieved. Furthermore, on-chip oscillator integration (crystal-less) provides low power consumption, small area, and comfortable wearing compared with quartz crystal. The clock calibration methodology is proposed to combat the large frequency offset of on-chip oscillator. With calibration methodology, clock offset tolerance can achieve up to 2%.

Emulation platform includes TX front-end, RX front-end, and TRX baseband. TRX baseband is implemented in FPGA, which contains OFDM system and proposed clock calibration methodology. The emulation platform provides reliable transmission with 6.7Mbps data rate. Compared with other BCC systems, our proposal achieve high data rate with better spectral efficiency, and on chip oscillator integration to provide smaller area and more comfortable wearing.

6-2 Future Work

In the future, we are going to achieve much higher data rate. There are some approaches to improve the data rate. First is to include error-correcting code (ECC) to provide better BER performance. Convolutional code, turbo code, or even low-density parity-check code (LDPC) could be candidates for the system. Secondly, as mentioned in Chapter 2, human body exists body antenna effect, thus environmental interference couples to the body, which degrades the signal quality. Therefore, we should develop a way to combat this problem in order to improve data rate.

Reference

[1] S.-J. Song, N. Cho, and H.-J. Yoo, “A 0.2 mW 2 Mb/s digital transceiver based on wideband signaling for human body communications,”IEEE J. Solid-State Circuits, vol. 42, no. 9, pp. 2021–2033, Sep. 2007.

[2] N. Cho, L. Yan, J. Bae, and H.-J. Yoo, “A 60 kb/s–10 Mb/s adaptive frequency hopping transceiver for interference-resilient body channel communication,” IEEE J. Solid-State Circuits, vol. 44, no. 3, pp.708–717, Mar. 2009.

[3] N. Cho, J. Bae, and H.-J. Yoo, “A 10.8 mW body channel communication/MICS dual-band transceiver for a unified body sensornetwork controller,” IEEE J. Solid-State Circuits, vol. 44, no. 12, pp.3459–3468, Dec. 2009.

[4] A. Fazzi, S. Ouzounov, and J. Homberq, “A 2.75 mW wideband correlation-based transceiver for body-coupled communication,” in 2009 IEEE Int. Solid-State Circuits Conf. Dig. Tech. Papers, Feb. 2009, pp.204–205.

[5] J. Bae, K. Song, H. Lee, L. Cho, H.-J. Yoo, “A 0.24-nJ/b Wireless Body-Area-Network Transceiver With Scalable Double-FSK Modulation,” IEEE J. Solid-State Circuits, vol. 47, no. 1, pp.310–322 Jan. 2012.

[6] C. Y. Yu, J.Y. Yu, and C. Y. Lee, "An eCrystal oscillator with self calibration capability," IEEE International Symposium on Circuits and Systems (ISCAS), pp. 237-240, May 2009

[7] Nakata, A. , et al, " Development and Performance Analysis of An Intra-body Communication Device," in 12th International Conference on TRANSDUCERS, Solid-State Sensors, Actuators and Microsystems, SENSOR’03, Vol. 2, Aug 2003, pp. 1722 – 1725.

[8] Shu-Yu Hsu, Jui-Yuan Yu, Chien-Ying Yu, and Chen-Yi Lee Wei-Hao Sung, "A Frequency Accuracy Enhanced Sub-10μW On-chip Clock Generator for Energy Efficient Crystal-less Wireless Biotelemetry Applications," in IEEE Symposium on VLSI Circuits Dig. Tech. Papers, Jun. 2010, pp. 115-116.

[9] Jui-Yuan Yu, Ching-Che Chung, Wan-Chun Liao, and Chen-Yi Lee, "A sub-mW multi-tone CDMA baseband transceiver chipset for wireless body area network applications," in ISSCC Dig. Tech. Papers, 2007, pp. 364-365.

[10] Wei-Hao Sung, Jui-Yuan Yu, and Chen-Yi Lee, "A Robust Frequency Tracking Loop for Energy-Efficient Crystalless WBAN Systems," IEEE Transactions on Circuits and Systems-II (TCAS-II), vol. 58, no. 10, 2011.

[11] Tsan-Wen Chen, Ping-Yuan Tsai, Jui-Yuan Yu, and Chen-Yi Lee, "A Sub-mW All-Digital Signal Component Separator with Branch Mismatch Compensation for LINC Transmitters," IEEE Journal of Solid-State Circuits (JSSC), vol. 46, no. 11, pp. 2514-2523, Nov. 2011.

[12] Tsan-Wen Chen, Jui-Yuan Yu, Chien-Ying Yu, and Chen-Yi Lee, "A 0.5 V 4.85 Mbps Dual-Mode Baseband Transceiver With Extended Frequency Calibration for Biotelemetry Applications," IEEE Journal of Solid-State Circuits (JSSC), vol. 44, pp. 2966-2976, Nov. 2009.

[13] Long Yan, Joonsung Bae, and Hoi-Jun Yoo, "A 1Mb/s, -75dBm Sensitive Fully Integrated Body Channel Transceiver for a Low Energy Compact Wearable Healthcare Sensor," in ASSCC, 2010, pp. 1-4.